Ore Geology Reviews 80 (2017) 923–946

Contents lists available at ScienceDirect

Ore Geology Reviews

journal homepage: www.elsevier.com/locate/oregeorev

The Xitieshan volcanic sediment-hosted massive sulfide deposit, North Qaidam, China: Geology, structural deformation and geochronology

Jiangang Fu [a,b], Xinquan Liang [a,*], Ce Wang [a], Yun Zhou [c], Ying Jiang [a], Chaoge Dong [a]

[a] State Key Laboratory of Isotope Geochemistry, Guangzhou Institute of Geochemistry, Chinese Academy of Sciences, 511 Kehua Street, Tianhe District, Guangzhou, China
[b] Chengdu Institute of Geology and Mineral Resources, China Geological Survey, Chengdu, Sichuan, China
[c] College of Earth Sciences, Guilin University of Technology, Guilin, Guangxi, China

ARTICLE INFO

Article history:
Received 13 March 2016
Received in revised form 23 August 2016
Accepted 24 August 2016
Available online 26 August 2016

Keywords:
Structural deformation
Geochronology
Xitieshan deposit
North Qaidam

ABSTRACT

The Xitieshan deposit (~64 Mt at 4.86% Zn, 4.16% Pb, 58 g/t Ag, and 0.68 g/t Au) is hosted by the Middle to Late Ordovician Tanjianshan Group of the North Qaidam tectonic metallogenic belt, NW China. This belt is characterized by island arc volcanic, ultra-high pressure (UHP) metamorphic and ophiolitic rocks. The Tanjianshan Group constitutes a succession of metamorphosed bimodal volcanic and sedimentary rocks, which are interpreted to have formed on the margin of a back-arc ocean basin between the Qaidam block and the Qilian block.

Four stratigraphic units are identified within the Ordovician Tanjianshan Group. From northeast to southwest they are: 1) unit a, or the lower volcanic-sedimentary rocks, comprising bimodal volcanic rocks (unit a-1) and sedimentary rocks (unit a-2) ranging from carbonates to black carbonaceous schist; 2) unit b, or intermediate-mafic volcaniclastic rocks, characterized by intermediate to mafic volcaniclastic rocks intercalated with lamellar carbonaceous schist and minor marble lenses; 3) unit c, a purplish red sandy conglomerate that unconformably overlies unit b, representing the product of the foreland basin sedimentation during the Early Silurian; 4) unit d, or mafic volcanic rocks, from base to up, comprising the lower mafic volcaniclastic rocks (unit d-1), middle clastic sedimentary rocks (unit d-2), upper mafic volcaniclastic rocks (unit d-3), and uppermost mafic volcanic rocks (unit d-4). Unit a-2 hosts most of the massive sulfides whereas unit b contains subordinate amounts.

The massive stratiform lenses constitute most of the Xitieshan deposit with significant amount of semi-massive and irregularly-shaped sulfides and minor amounts in stringer veins. Pyrite, galena and sphalerite are the dominant sulfide minerals, with subordinate pyrrhotite and chalcopyrite. Quartz is a dominant gangue mineral. Sericite, quartz, chlorite, and carbonate alteration of host rocks accompanies the mineralization.

U-Pb zircon geochronology yields three ages of 454 Ma, 452 Ma and 451 Ma for the footwall felsic volcanic rocks in unit a-1, sedimentary host rocks in unit a-2 and hanging-wall unit b, respectively. The Xitieshan deposit is considered to be coeval with the sedimentation of unit a-2 and unit b of the Tanjianshan Group. The Xitieshan deposit has been intensely deformed during two phases (main ductile shear and minor ductile-brittle deformation). The main ductile shear deformation controls the general strike of the ore zones, whereas minor deformation controls the internal geometry of the ore bodies. ^{40}Ar-^{39}Ar age of muscovite from mylonitized granitic gneisses in the ductile shear zone is ~399 Ma, which is interpreted to date the Xitieshan ductile shear zone, suggesting that Early Devonian metamorphism and deformation post-dated the Tanjianshan Group.

The Xitieshan deposit has many features similar to that of the Bathurst district of Canada, the Iberian Pyrite Belt of Spain, the Wolverine volcanogenic massive sulfide deposit in Canada. Based on its tectonic setting, host-rock types, local geologic setting, metal grades, geochronology, temperatures and salinities of mineralizing fluid and source of sulfur, the Xitieshan deposit has features similar to sedimentary exhalative (SEDEX) and VMS deposits and is similar to volcanic and sediment-hosted massive sulfide (VSHMS) deposits.

1. Introduction

The Xitieshan Pb-Zn deposit is located in the eastern part of Qinghai province, approximately 80 km southeast of town Dachaidan, NW China (Fig. 1A). It is one of the largest Pb-Zn deposits in China. The deposit contains 64 million tonnes (Mt) of ore in reserves and geologic resources, at an average grade of 4.86% Zn, 4.16% Pb, 58 g/t Ag, and 0.68 g/t Au (Hou et al., 1999; Wang et al., 2013). The main orebody is approximately 150–250 m long, 50 m wide, at least 3–4 m (locally up to 30 m) thick. The deposit is hosted in the Ordovician Tanjianshan Group, and located in the middle part of the North Qaidam tectonic belt (Fig. 1A and B), which is one of the major Paleozoic polymetallic

* Corresponding author at: Guangzhou Institute of Geochemistry, Chinese Academy of Sciences, 511 Kehua Street, Tianhe District, Guangzhou 510640, Guangdong Province, China.
E-mail address: liangxq@gig.ac.cn (X. Liang).

http://dx.doi.org/10.1016/j.oregeorev.2016.08.027
0169-1368/© 2016 Published by Elsevier B.V.

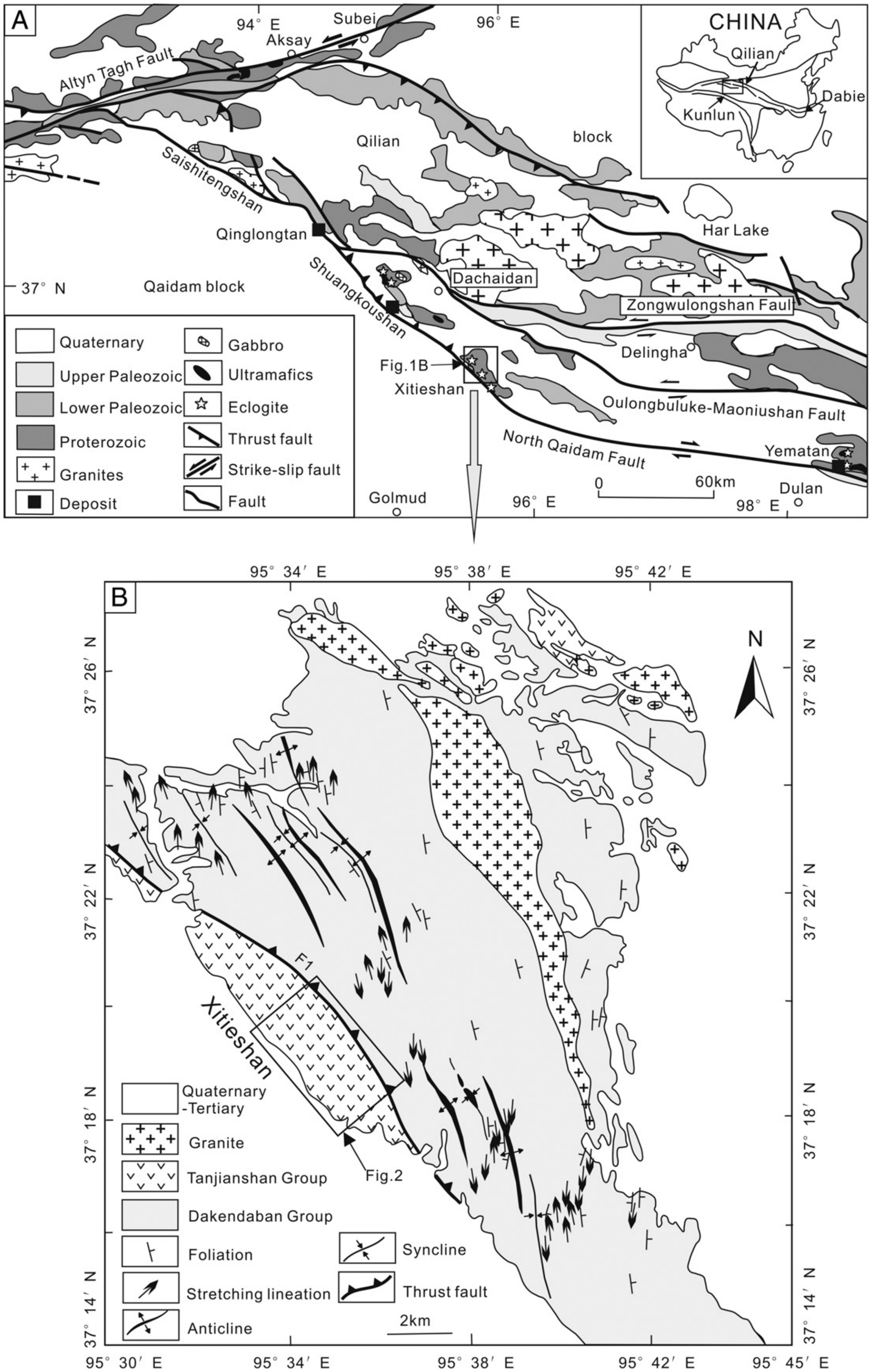

Fig. 1. A. Simplified regional geologic map, showing the location of the study area in the northwestern China. B. Map showing the distribution of the Tanjianshan and Dakendaban groups, and the location of Fig. 2. Map modified from Xu et al. (2006) and Zhang et al. (2009).

metallogenic belts of the Tibetan Plateau in NW China (Wang et al., 2003).

In recent years, several general reviews of the Xitieshan VMS deposit were published. These works included studies of stratigraphy, geologic setting, and genesis of the deposit (Feng et al., 2010; Wu et al., 1987; Wu et al., 2010; Zhang et al., 2005), a study of the genesis and exploration significance of hydrothermal sedimentary rocks (Li et al., 2009), and the sources of ore-forming fluid (Wang et al., 2009; Wang et al., 2008; Zhu et al., 2010). However, detailed descriptions are limited, and many geologic parameters, critical for ore formation, are unknown. Poor knowledge of the stratigraphy, absence of precise U-Pb chronology, and poor understanding of the deformation history (especially the age of the shear zone formation), are typical for the Xitieshan deposit. These aspects also have implications for exploration for similar deposits elsewhere in North Qaidam.

The objectives of this paper are: 1) to provide a descriptive field-based geologic database of the Xitieshan deposit, to enable comparison with other mid-Paleozoic VMS deposits in North Qaidam and elsewhere in the world; 2) to understand the timing of Xitieshan VMS mineralization in the volcanic-sedimentary rocks; 3) to provide temporal constraints on the ductile shear deformation and associated mineralization in the Xitieshan district; 4) to elucidate the relationship among the sedimentation, mineralization and volcanism in the Xitieshan deposit; and 5) to provide insight into the genesis of the Xitieshan deposit.

2. Regional geologic setting

The North Qaidam tectonic belt is located at the northeastern margin of the Tibetan Plateau, NW China (Fig. 1A). It is characterized by the development of Paleozoic island arc volcanic rocks, HP-UHP metamorphic rocks and ophiolite complexes (Shi et al., 2006; Yang et al., 2006). The belt extends for about 400 km long in a NNW direction, which is in fault contact with the Qaidam block to the southwest and the Qilian block to the northeast, along the North Qaidam fault and Zongwulongshan fault, respectively (Fig. 1A). The North Qaidam tectonic belt is offset by the sinistral Altyn Tagh fault in the northwest (Fig. 1A), and is cut by the Elashan fault in the east (Tang et al., 2002). A Cenozoic intra-continental sedimentary basin (Qaidam basin) overlain the Precambrian crystalline basement and the Paleozoic fold belt (part of the Qaidam block) (Bureau of Geology Mineral Resources of Qinghai Province, 1991). The Qilian block consists predominantly of Precambrian orthogneiss, paragneiss, schist and marble, and overlying Paleozoic sedimentary rocks, with depositional contact (locally faulted) (Wan et al., 2001).

The North Qaidam tectonic belt is comprised predominantly of Precambrian orthogneiss and paragneiss, amphibolite, mafic granulite and marble intercalated with minor slices of eclogite and garnet peridotite (Zhang et al., 2008). They are in fault contact with the lower Paleozoic Tanjianshan Group and intruded by the Silurian granite (ca. 428 Ma) (Meng et al., 2005). The Tanjianshan Group occupies a northwest trending band, approximately 1–2 km wide, which discontinuously distributes in Saishitengshan, Shangkoushan, Xitieshan and Dulan areas from northwest to northeast (Fig. 1A). It is mainly composed of deformed and metamorphosed, lower greenschist to amphibolite facies metasedimentary and metavolcanic rocks (Fig. 1; Wu et al., 1987).

The North Qaidam orogen is one of the most important polymetallic belts in the northwest of China (Mao et al., 2003). Many massive sulfide deposits are hosted in the lower Paleozoic volcanic-sedimentary rocks of the Tanjianshan Group in this belt, such as the Qinglongtan, Shuangkoushan and Xitieshan Pb-Zn massive sulfide deposits (Fig. 1A).

3. Local geologic setting

In the Xitieshan district, the Dakendaban Group in the northeast is in structural contact with underlying younger volcanic-sedimentary rocks of the Tanjianshan Group in the southwest (Figs. 1B and 2). The Tanjianshan Group, hosting most of the Xitieshan massive sulfide deposits, has been divided into four informal units from northeast to southwest; they are: 1) unit a, or the lower volcanic-sedimentary rocks, comprising bimodal volcanic rocks (unit a-1) and sedimentary rocks (unit a-2); 2) unit b, or intermediate-mafic volcaniclastic rocks; 3) unit c, a purplish red sandy conglomerate; 4) unit d, or mafic volcanic rocks, from base to up, comprising the lower mafic volcaniclastic rocks (unit d-1), middle clastic sedimentary rocks (unit d-2), upper mafic volcaniclastic rocks (unit d-3), and uppermost mafic volcanic rocks (unit d-4) (Figs. 2, 3 and 4) (Wu et al., 1987; Zhang et al., 2005). The tectonic setting of the Tanjianshan Group was interpreted to be either a Middle-Late Ordovician intra-continental rift (Wu et al., 1987), as well as island arc and/or back-arc basin (Wu et al., 2010). The Dakendaban Group is laterally extensive and mainly composed of Neoproterozoic para- and orthogneiss (Fig. 3), with minor amphibolite, mafic granulite, marble, and locally eclogite and garnet peridotite (Zhang et al., 2009).

The area of the Xitieshan mine was strongly deformed during Middle Paleozoic times (about 440–400 Ma) (Guo, 2000; Wang et al., 2000). Two obvious deformation phases have been recognized: early main ductile deformation and late minor brittle-ductile deformation. Predominant ductile deformation resulted from the oblique continent-continent collision between the Qaidam and Qilian blocks, and produced a regional ductile shear in North Qaidam. It was then overprinted by minor brittle-ductile deformation. This regional deformation event resulted in the oblique subduction of the Tanjianshan Group from SW to NE, which underlie the Dakendaban Group (Fig. 3), and the formation of the Xitieshan ductile shear zone.

The sequence of the Tanjianshan Group in the Xitieshan mining area was exposed to low- to moderate-grade regional metamorphism ranging from lower greenschist to middle amphibolite facies, with mineral assemblage of sericite, actinolite, albite, chlorite, amphibole, and biotite. Four main alteration styles were recognized at the Xitieshan deposit, including silica (quartz), carbonate, chlorite, and sericite alteration. Hydrothermal alteration zones occur beneath, lateral to, and within massive and stringer vein sulfide zones. However, the hydrothermal alteration model related to mineralization has not been clearly established.

4. Deposit stratigraphy

The sequence of the Tanjianshan Group overall includes two volcanic-sedimentary cycles from bottom to top: the first cycle consists of units a and b, whereas the second cycle is unit d. The Xitieshan deposit is confined to the lower part of the Tanjianshan Group (Figs. 3, 4). The main characteristics of each unit in the Tanjianshan Group are summarized as follow, from northeast to southwest:

4.1. Unit a, lower volcanic-sedimentary rocks

4.1.1. Unit a-1, mafic-felsic bimodal volcanic rocks

Owing to the late structural deformation, unit a-1 structurally underlies granitic gneiss of the Dakendaban Group (Fig. 3). Unit a-1 is subdivided into three parts from base to top (Fig. 5) and is characterized by bimodal volcanic rocks (Fig. 6A). The lower part, about 40 m thick, is composed of meta-mafic volcanic rocks, volcaniclastic rocks, fine-grained quartz sandstone and lamellar exhalite (barite, quartz and minor calcite) with minor carbonaceous argillite at the bottom. The middle part of unit a-1 comprises predominantly rhyolite porphyry (Fig. 6A, B, C and D), interbedded with chlorite schist, and siliceous rock. Potassium feldspar-phyric rhyolite bodies, ranging in thickness from 5 to 8 m, occur approximately 300 m below the massive sulfide lenses in this unit. Potassium feldspar, plagioclase, and minor quartz phenocrysts are present, all somewhat elongated because of deformation effects (Fig. 6C). These felsic volcanic rocks are calc-alkaline dacite and rhyolite, and their geochemical characteristics are similar to that of FII-type rhyolite in the other VMS deposits elsewhere (Gaboury and Pearson, 2008; Hart et al., 2004; Lentz, 1998; Lesher et al., 1986; Sun

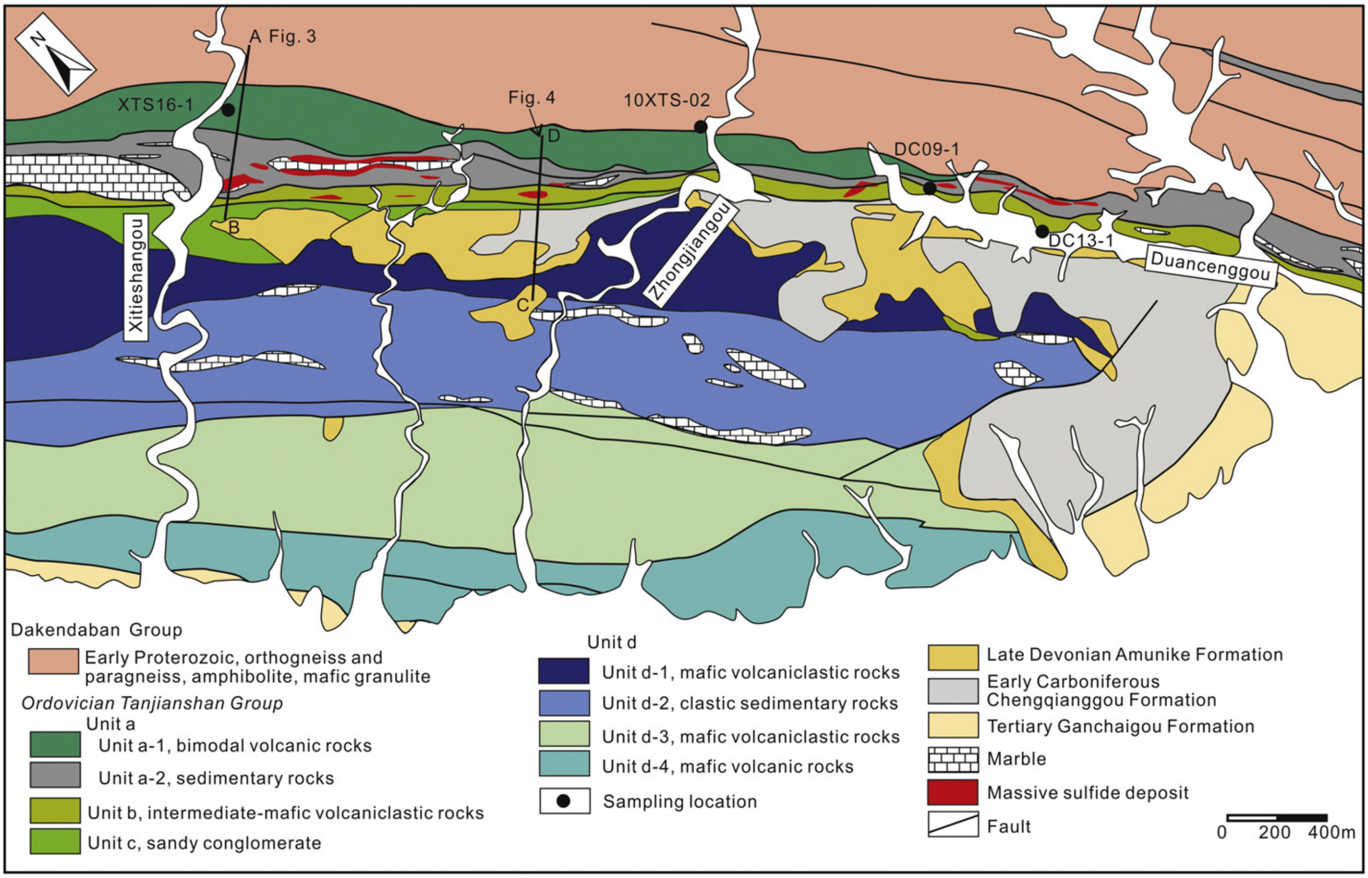

Fig. 2. Geologic map of the Xitieshan deposit area, showing the distribution of rock units with respect to the massive sulfide deposits. Map modified from the Xitieshan prospecting report (2009) (unpublished map).

et al., 2012). The upper part of unit a-1, several meters in thickness, is composed of thinner black carbonaceous argillite, interbedded with mafic volcanic rocks (Fig. 6A, E) and minor fine grained sandstone.

4.1.2. Unit a-2, sedimentary rocks

This unit is the principal host rock for mineralization. It is predominantly composed of black carbonaceous argillite, marble and massive sulfide lenses, veins, with minor chlorite schist and volcaniclastic rocks at the top and exhalite at the base (Fig. 5). The thickness of unit a-2 is greatest near the center of the deposit; it decreases towards the sides and along strike, which is consistent with the massive sulfides thickness, speculating that the thickest host rocks maybe correspond to the center of the sedimentary basins or the location of a syngenetic fault (Zhang et al., 2005). Excluding the massive sulfides, unit a-2 contains three main rock types: schists, marble, and hydrothermal sedimentary rocks.

The schists include calcareous schist, carbonaceous schist, quartz schist, and chlorite-amphibole schist. The calcareous schist is characterized by a light gray color, lepidoblastic texture, and schistose structure. It consists of calcite, chlorite, and minor quartz. The carbonaceous schist is composed of quartz, sericite, chlorite and plagioclase, about 100 m thick, overall black green in color, and commonly has disseminated pyrite. The quartz schist is dominantly composed of quartz, plagioclase, sericite, and chlorite with subordinate actinolite and epidote. The

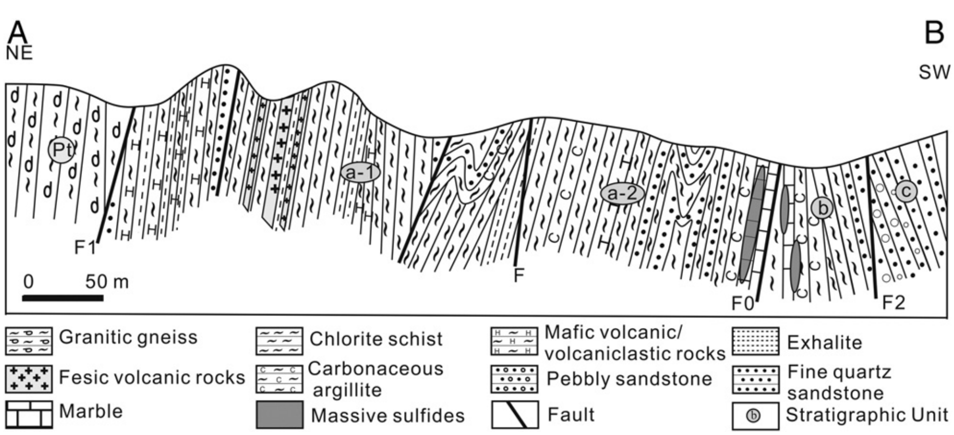

Fig. 3. Geologic cross section (A-B, location shown in Fig. 2) through the Xitieshangou zone of the Xitieshan deposit.

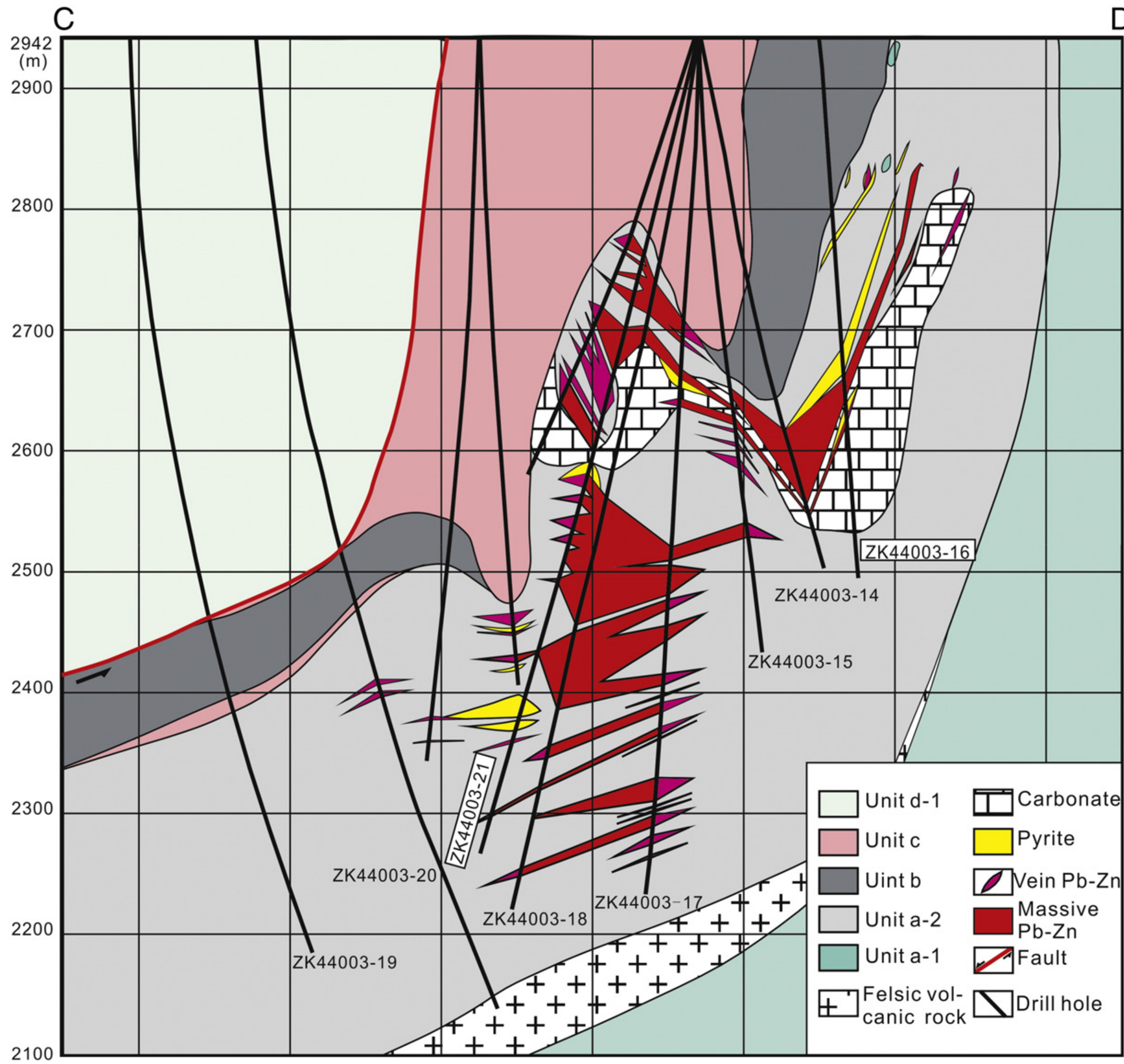

Fig. 4. Geological section along 03 exploration line of the Xitieshan Pb-Zn deposit, location in Fig. 2, showing the relationship between the felsic volcanic rocks and massive sulfide deposits, the morphology of ore body was transformed by the late ductile shear deformation, resulting in a series of variational lenticle forms. All the drill holes were opened at the level 2942 m. Diagram modified from the Xitieshan prospecting report (2009) (unpublished sections).

chlorite-amphibole schist is minor, and is composed of amphibole, chlorite, and minor quartz.

The marble is grayish white, and made of fine grained, lamellar, or banded carbonates. It exhibits mosaic or granoblastic texture, and consists of calcite (ca. 90%) and minor quartz. Quartz particles, typically characterized by the clastic structure, are rounded, cemented by calcite, and likely deposited in a shallow sea sedimentary environment. Iron-manganese marble occurs extensively in the northwest of the deposit.

Hydrothermal sedimentary rocks extensively occur in unit a-2 and include five types: siliceous marble, siliceous rocks, cryptoexplosion breccias, zinc-rich siderite and gypsum rocks, and rhodochrosite-rich rocks. Most siliceous marble occurs under the ore horizon. It is light gray-white in color, and composed predominantly of fine-grained calcite and quartz laminae (ca. 0.1–0.3 cm thickness). Siliceous rocks, occuring as banded iron-manganese chert formation (Fig. 6F) in both the hanging wall and footwall, are gray to grayish-green in color, 3 to 25 cm in thickness, and contain minor chlorite and carbonaceous matter. Cryptoexplosion breccias comprise angular fragments of siliceous rock, carbonaceous schist, chlorite schist, quartz and fine-grained marble (Fig. 7A). The fragments are cemented by sulfides, siliceous, argillaceous, and carbonate matter (Fig. 7A, B). Based upon the multi centre, beaded distribution of cryptoexplosion breccias in a NW direction in unit a-2, hydrothermal-exhalation is inferred to have been controlled by a NW trending syndepositional fault. Zinc-rich siderite and gypsum veinlets, containing zinc-rich siderite and microcrystals of gypsum, mainly occur between stratiform massive sulfides and the marble host rocks, but also as veinlets in schist; these veinlets can be several mm to tens of mm in thickness. Overall, from bottom to top, the sequence of hydrothermal sedimentary rocks consist of cryptoexplosion breccia, siliceous rock, lamellar carbonate and gypsum, banded pyrite interlayered with siliceous rock, and banded sulfides, respectively (Zhang et al., 2005).

4.2. Unit b, intermediate-mafic volcaniclastic rocks

This unit is the minor ore-hosting rock. It contains marble with massive sulfides, carbonaceous argillite, mafic volcanic rocks, volcaniclastic rocks, sericitic quartzo-feldspathic clastic rocks, chlorite schist and carbonaceous argillite from base to top. The marble is characterized by lamellar and banded calcite, interbedded with banded chlorite, carbonaceous schist and biotite. Hydrothermal sedimentary rocks are not present either above or below of the massive sulfides in this minor host. This host rock, to a great extent, is similar to unit a-2, with

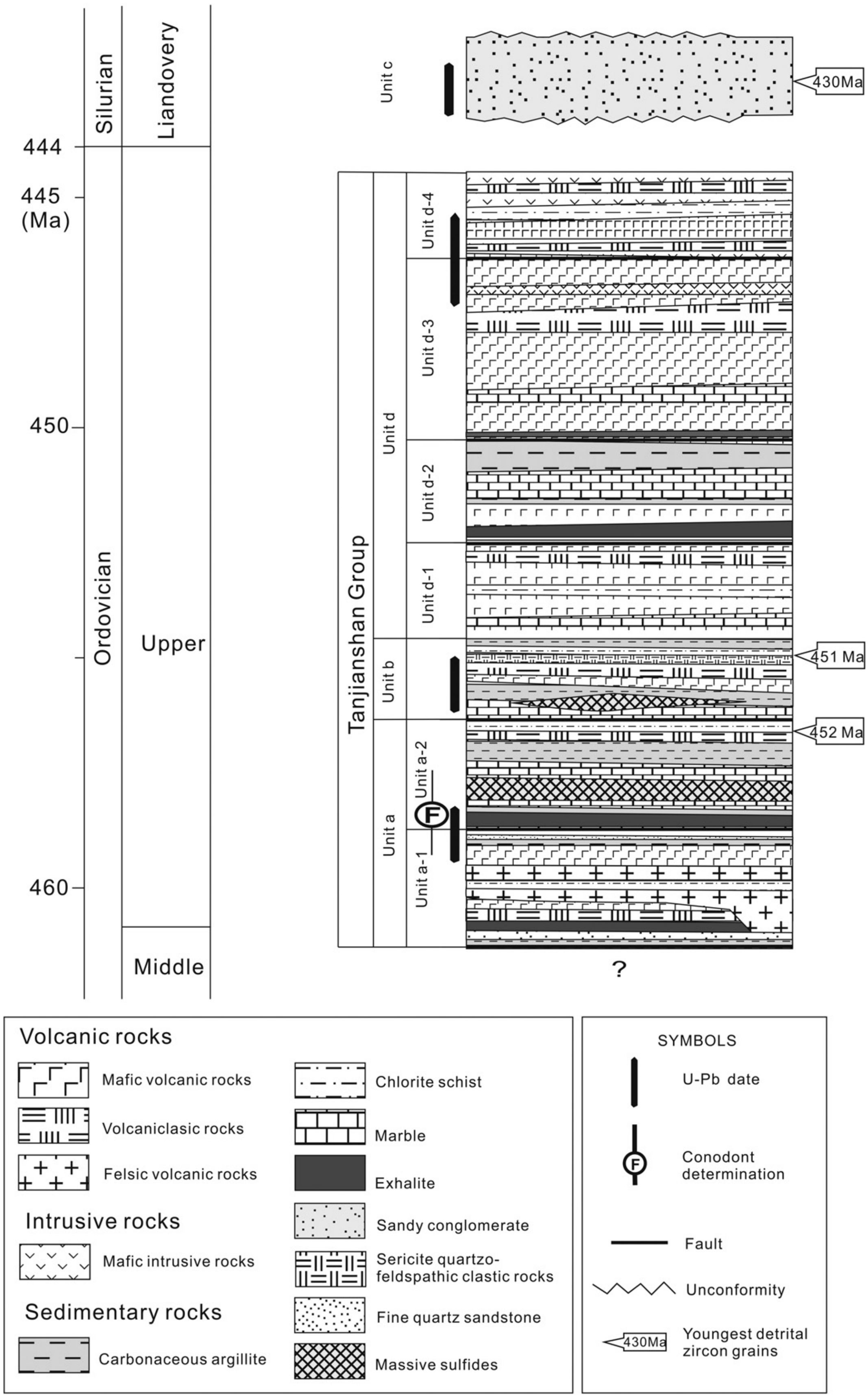

Fig. 5. Schematic stratigraphic column of the Tanjianshan Group in the Xitieshan district.

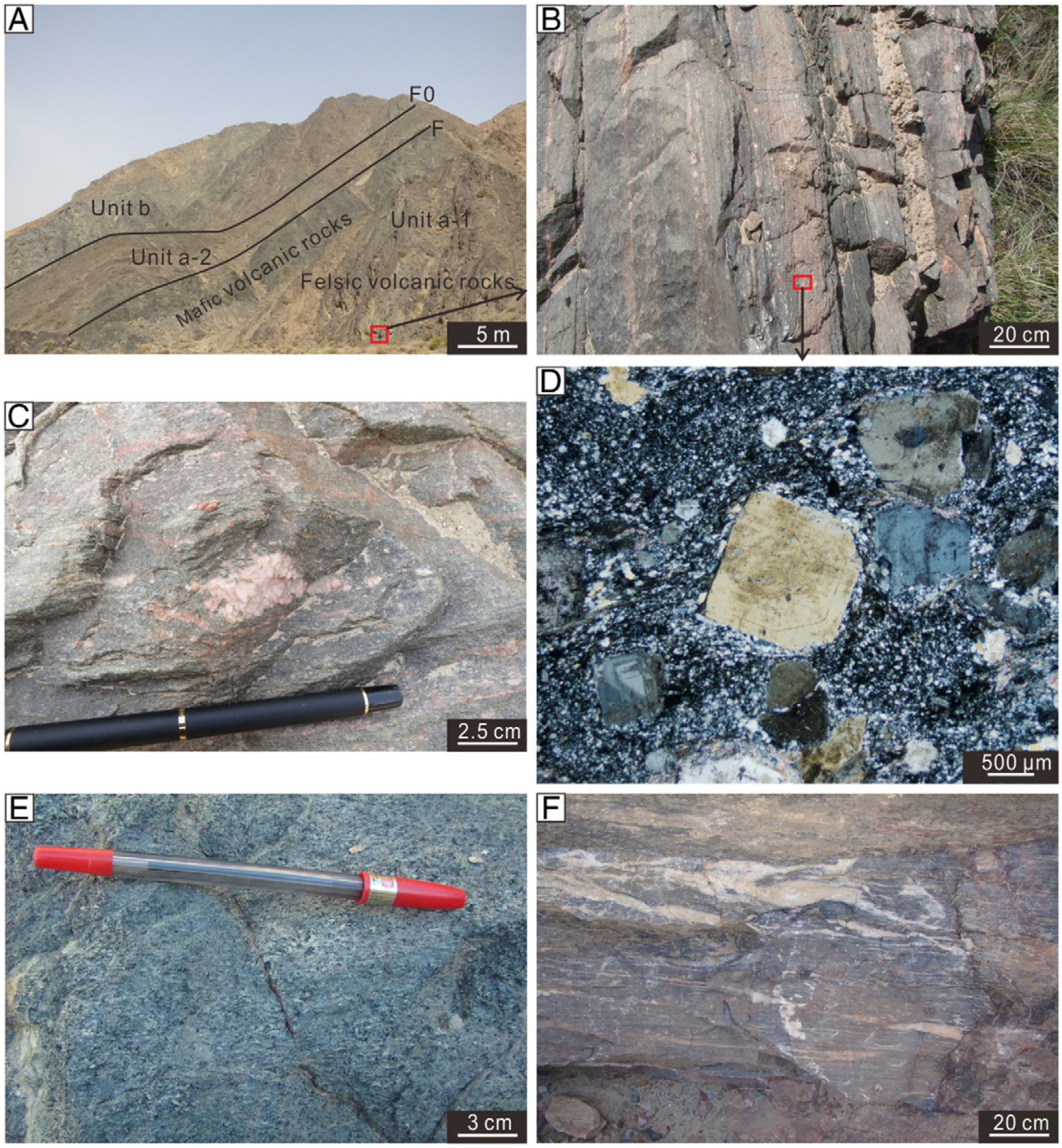

Fig. 6. A. The overall outcrop of the lower Tanjianshan Group, including units a-1, a-2 and b. B. Rhyolite porphyry that is interbedded with chlorite schist in unit a-1. C. The rotated and elongated feldspar phenocryst in rhyolite porphyry, unit a-2. D. Micrograph of the rhyolite porphyry in unit a-1 (X-polarized light). E. Mafic volcanic rock in unit a-1. F. Banded iron-manganese chert iron formation, interbedded with lamellar white marble in unit a-2.

the exception of the more volcaniclastic rocks than meta-sedimentary rocks, and higher content of chalcopyrite and gold.

4.3. Unit c, sandy conglomerate

Unit c crops out between units b and d, and appears to be a younger tectonic slice or unconformable block. It is mainly composed of weakly metamorphosed grayish-purple conglomerate, pebbly sandstone, feldspath-quartz sandstone and siltstone (Fig. 7C). The grain size of this conglomerate decreases from base to top, up to several centimeters to decimeters near the base. The clasts are poorly sorted and angular, and are composed of volcanic rocks, marble, and carbonaceous slate. This unit is locally overlain by the molassoid Late Devonian Amunike Formation (D_3a). In addition, we have dated the detrital zircons from unit c using the U-Pb LA-ICP-MS. The result suggests that the maximum sedimentary age is younger than 430 Ma (Fu et al., 2014), indicating that this unit is younger than the Tanjianshan Group and should be removed from the Tanjianshan Group (Fu et al., 2014). To some extent, it is interpreted as a product of the Early Silurian foreland sedimentary basin (Du et al., 2004).

4.4. Unit d, mafic volcanic rocks

4.4.1. Unit d-1, lower mafic volcaniclastic rocks

This unit unconformably overlies unit c. It is subdivided into a lower and an upper part. The lower part is composed of mafic volcanic rocks, chlorite schist, and thin marble. The chlorite schist has always suffered chlorite and sericite altered. The upper part is composed predominantly of meta-mafic volcanic rocks with minor volcaniclastic rocks near the top, which contains amphibole, actinolite, chlorite, and sericite. The geochemistry of unit d-1 corresponds to the oceanic island arc basalt (OIB) (Sun et al., 2012).

4.4.2. Unit d-2, clastic sedimentary rocks

This unit is predominantly composed of carbonaceous argillite, exhalite, marble and minor mafic volcanic rocks. Siliceous rocks and Fe-Mg chert occur near the base of this unit. In outcrops, unit d-2 is similar to unit a-2 in color, composition and lithological association. The mafic volcanic rocks of unit d-2 are tholeiitic in composition and very similar to MORB (Sun et al., 2012).

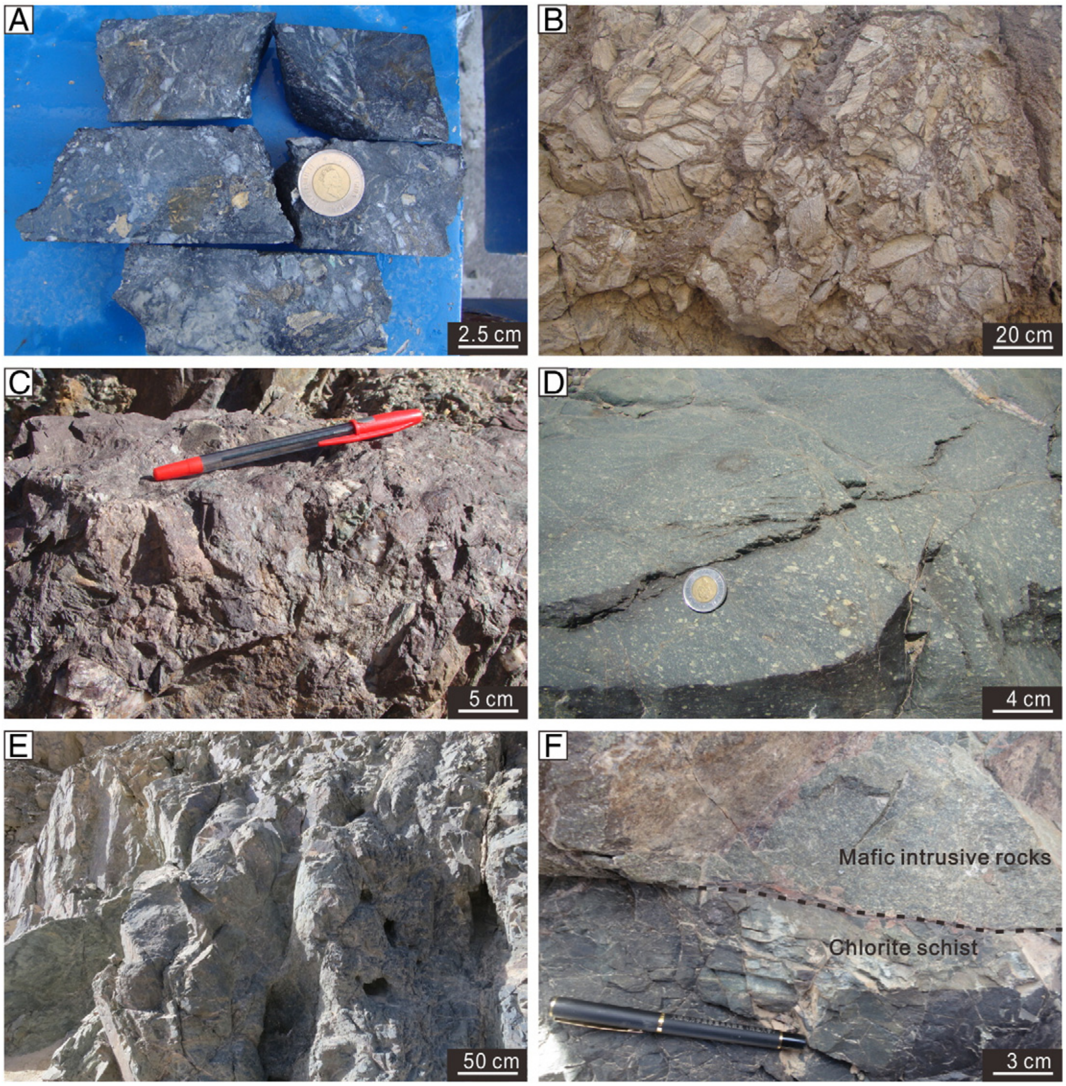

Fig. 7. A. Cryptoexplosion breccias from drill core ZK041-11 in unit a-2. B. Hydrothermal breccias in unit a-2. C. Purplish red conglomerate near the bottom of unit c. D. Mafic volcanic rocks with the amygdaloidal structure in unit d-3. Coin is 2.8 cm in diameter. E. Pillow structure of the volcanic lava in unit d-4. F. The late mafic intrusive rock invaded into the chlorite schist in unit d-4, the photo has been rotated 90° counterclockwise.

4.4.3. Unit d-3, upper mafic volcaniclastic rocks

Unit d-3 is predominantly composed of the dull gray-green mafic volcanic rocks, volcaniclastic rocks, exhalite, minor gray-green gabbro, and locally interlaid with minor banded marble. This unit is the thickest in the Xitieshan area, ranging from 300 to 650 m. The mafic volcanic rocks locally exhibit the amygdaloidal structure (Fig. 7D) and contain various amounts of amphibole, chlorite, biotite, feldspar and sericite. This unit is characterized by the presence of mafic volcanic rocks associated with gabbro, consistent with the second volcanic sedimentary circle, with volcanism gradually increased while the sedimentation quickly decreased during this period. It resulted in the presence of volcaniclastic rocks which were going to transform into the sedimentary rocks. The geochemistry of unit d-3 suggests a back-arc depositional environment (our unpublished data), which is somewhat between OIB and N-MORB (Hollings et al., 2000; Stolz, 1995; Taylor and Martinez, 2003).

4.4.4. Unit d-4, top mafic volcanic rocks

Generally, this unit, about 200 m in thickness, is similar to unit d-3 except for local pillow basalt (Fig. 7E). Unit d-4 is mainly composed of gray-green mafic volcanic rocks, volcaniclastic rocks, mafic intrusive rocks, and chlorite schist. Unit d-4 is also intruded by the late mafic intrusive rocks at the top (Fig. 7F), which ranges in thickness from several tens of centimeters to ca. 40 m.

5. Massive sulfide lenses

5.1. Massive stratiform sulfides

Massive stratiform sulfide lenses, comprising of 60 to 70 vol.% fine-grained (0.5–1 mm) sulfide minerals and ranging from several centimeters to 20 cm in thickness (Fig. 8A), are parallel to the S_1 foliation, within marble near the contact with unit b. Pyrite is the dominant sulfide mineral, with subordinate pyrrhotite, chalcopyrite, galena and sphalerite. Pyrite typically occurs as euhedral, subhedral, anhedral fine or coarse-grained porphyroblasts (Fig. 8B), ranging from 1 to 8 mm in size. Galena and sphalerite mainly occur as disseminations, cloddy, or intercalated with pyrite, pyrrhotite, silicalite, marble and schist. Quartz is the dominant gangue mineral, with subordinate carbonate. Fine-grained, reddish brown sphalerite form wispy bands parallel to the S_1 foliation, likely resulting from late tectonic deformation, and locally associated with subhedral pyrite and sporadically distributed chalcopyrite and galena (Fig. 8C). Most pyrite layers are deformed.

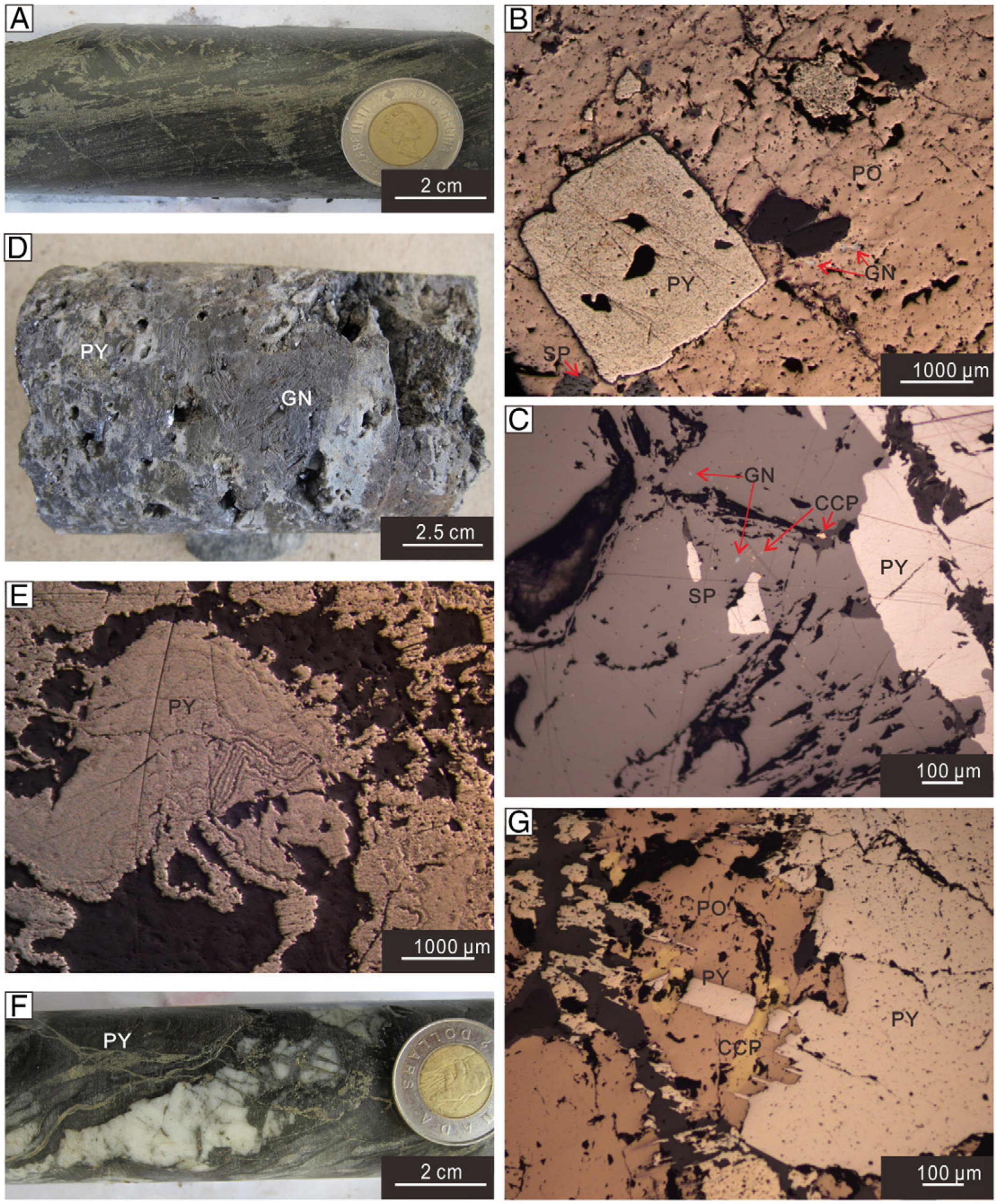

Fig. 8. A. Pyrite layers in drill core ZK041-11. Coin is 2.8 cm in diameter. B. Micrograph showing euhedral, coarse-grained pyrite in pyrrhotite in drill core ZK44003-18 (Nonpolarized, reflected light). C. The subhedral pyrite and sporadically distributed chalcopyrite and galena in sphalerite in drill core ZK44003-18. D. Massive sulfides with vesicular structure in drill core ZK81-12. E. Micrograph showing the typical structure of pyrite in drill core ZK44003-21 (Nonpolarized, reflected light). F. Stringer vein sulfides in drill core ZK041-11. Coin is 2.8 cm in diameter. G. Micrograph showing pyrite, pyrrhotite and chalcopyrite in drill core ZK44003-18 (Nonpolarized, reflected light). Abbreviations as follow: PY = pyrite, SP = sphalerite, CCP = chalcopyrite, PO = pyrrhotite, and GN = galena.

In unit a-2, bands of massive sulfides are intercalated with schist, over approximately 20–60 m in total thickness. Pyrrhotite is the dominant sulfide mineral, with lesser pyrite. Pyrite is fine-grained and loose in structure, probably representing product of recrystallization of colloform pyrites. It is locally replaced by sphalerite, forming the island-shape. In places pyrite forms cube-shaped porphyroblasts and aggregates of small phenocrysts, suggesting that massive sulfide deposit had been metamorphosed and hydrothermally altered. Galena and sphalerite display either irregular blebs or disseminations, together with subordinate pyrrhotite. This style of mineralization is commonly associated with the alteration minerals sericite and ankerite, which are best developed distal to the massive sulfide lenses.

5.2. Semi-massive and irregular nodular sulfides

Semi-massive and lenses of irregular nodular to framboidal sulfides in marble breccias constitute the main lens of the Xitieshan deposit currently. These orebodies range in size from several centimeters up to 10 m, and exhibit typically vesicular structure (Fig. 8D) which likely resulted from the late hydrothermal leaching. Pyrite, galena and sphalerite are the dominant sulfide minerals, with subordinate pyrrhotite, magnetite, marcasite, chalcopyrite, arsenopyrite and magnetite, and few electrum and stannite. Sphalerite occurs as coarse-grained euhedral porphyroblasts, which are not likely resulted from tectonic deformation. Pyrite is characterized by the embayment shape in the marble

(Fig. 8E), with $\delta^{34}S$ values ranging from 3.8 to 5.4 per mil (Zhu et al., 2010). Calcite is the common gangue mineral, with the high estimated salinities (12–18 wt.% NaCl equiv.) in carbonate rocks (Wang et al., 2009). There is a clear boundary between irregular nodular ore and the host marble. The marble commonly has embayed boundaries and locally forms residual islands in the sulfide. Replacement pieces of marble occur as anhedral in the sulfide orebodies, forming the concave embayment. Metal zoning occur near the boundary marble, from galena in the inner part, through sphalerite in transition to outer pyrite. Pyrite generally displays earlier precipitation than sphalerite and galena under acidic condition (Large, 1992). Whereas an acidic fluid is neutralized by the dissolution of carbonate, lead and zinc will be precipitate before iron sulfides.

5.3. Stringer vein sulfides

The sulfide-stringer veins are always associated with small faults or fractures in the rocks of the lower Tanjianshan Group, with great thickness in the east increasing with depth. Multiple stringer veins occurred at the different places, and formed the coalesced hydrothermal vent sites under the massive sulfide deposit. Stringer-sulfide zones in unit b are predominantly comprised of pyrite, with subordinate galena, sphalerite, chalcopyrite and pyrrhotite (Fig. 8F). The pyrite phenocryst was interrupted and replaced by the younger chalcopyrite (Fig. 8G). An average $\delta^{34}S$ value of 0.8 per mil CDT in pyrite represents the deep source of the ore-fluid as well (Zhu et al., 2010). Quartz is the dominant gangue mineral. The host rocks are altered, including silicification and carbonate alteration inside stringer veins, chloritization and sericitization near the host rocks. Ore-bearing quartz veins are elongated along the direction of schistosity, and form boudins or boudinage structure. On the other hand, stringer vein sulfides in unit a-2 are nearly vertical, range in width from 5 to 80 mm. They either intersect the bedding at a high angle or are parallel to it. Silicification is the dominant hydrothermal alteration, with subordinate chlorite and sericite alteration, and relatively weak carbonate alteration. Galena and sphalerite are the dominant sulfide minerals, with subordinate pyrrhotite and pyrite. Pyrrhotite includes both hexagonal and monoclinic varieties that are typical of hydrothermal deposits. The early pyrrhotite and recrystallized pyrite were always replaced by galena and sphalerite when the vein cuts the strata.

6. Deformation in the Xitieshan deposit area

Two generations of deformation were identified: 1) early main ductile deformation, mainly forming the mylonitized schistosity (Fig. 9A), small and intermediate size fold (Fig. 9B and C) and mullion structure (Fig. 9D); 2) late minor brittle-ductile deformation, forming kink bands (Fig. 9E) or two conjugate fracture cleavages (Fig. 9F).

6.1. Main ductile deformation

The main ductile deformation event, responsible for the formation of the main fabrics developed in the Xitieshan area and elsewhere, is attributed to regional deformation which resulted in the formation of the Xitieshan ductile shear zone between the lower Tanjianshan Group and the Dakendaban Group, which was overprinted by the late brittle fault F1 (Figs. 1B and 3). It trends NWW and dips at high angle to NE.

In the Xitieshan mining area, the coarse-grained granitic gneiss at the bottom of the Dakendaban Group has become granitic mylonite, super-mylonite or mylonite schist (Figs. 9A, 10A). These mylonites are characterized by a well-developed, penetrative schistosity and a conversion of feldspars to muscovite and quartz, muscovite replacement of biotite, and biotite replacement of amphibole. In the Tanjianshan Group, greenschist facies rocks in units a and b are overall interpreted as mylonite which include felsic (Fig. 10B), calcic and amphibolic mylonite (Feng et al., 1997). S-C fabric, the snapped (Fig. 10C), δ type and rotated phenocrysts (Fig. 10D and E), and shear lenses (Fig. 10F) are commonly present in these rocks. Different shear actions caused the imbalance of strain strength in the ductile shear zone, formed both strongly and weakly deformed regions (Fig. 11A and B), and exhibited the grid and/or podiform tectonic patterns (Fig. 11C and D). These different strain zones not only controlled the orebodies scales and forms, but also resulted in the change of the orebodies type (i.e. marble-hosted, schist-hosted, and transitional-hosted) (Fig. 11D, E and F). However, the formation age of this shear zone in the mining area is unknown so far. Both northwest and southeast-trending stretching lineations are commonly present in the schistosity plane, with a dominant northwest-trending (Figs. 1B and 12). The schistosity mostly parallels to the bedding in the Tanjianshan Group, trends north-west and dips steeply southwest or northeast (Fig. 12). The main schistosity intersects with bedding only at the hinge zone of a fold, and mostly coplanar with the bedding. Many small and intermediate size folds and mullion structures extensively occur in the main ductile deformation zone (Fig. 9B, C and D), and range from several centimeters to meters. These folds are generally confined to corridors as asymmetric or symmetric small tight folds, S- and sometimes *Z*-shaped folds, in which the axial plane is either coplanar to the cleavage or parallel to the schistosity.

Dynamic evidences for the ductile shear deformation, including the asymmetric folds, S-C fabric, rotated phenocrysts, mica fish structures, flattening and/or stretching of geologic markers, suggest that it is kinematically characterized by dextral compressional shear, and the Dakendaban Group obliquely thrusted from northeast to southwest. This main deformation event controlled the general shape of the ore zones at the Xitieshan deposit, which exhibit a series of lenses.

6.2. Minor brittle-ductile deformation

The minor brittle-ductile deformation is characterized by kink bands and two groups of conjugate brittle or brittle ductile fractures (Fig. 9E and F), likely originated from the Early to Middle Devonian orogeny (Guo, 2000). One group trends southeast and plunges to the northeast, whereas other group trends northwest and steeply dips. The intersecting line between two groups of ductile shear foliation represents the nearly horizontal intermediate stress axes ($\sigma 2$), northeast-trending, about 45°, while the subhorizontal compress stress axes ($\sigma 1$) trend northwest. This shows that the minor deformation resulted from superimposed subhorizontal compression from northwest to southeast, although the amount of compression is limited. The minor structural deformation controlled the internal geometry of the ore bodies, as exemplified by the cleavage and the conjugate fractures, and resulted in the change of the continuity of individual orebodies inside (Wang et al., 2000).

7. Geochronology

7.1. Host assemblage ages

The Rhenium (Re) content in pyrite is too low (only up to ppb levels) to be directly used for the *Re*-Os dating (our unpublished data). In order to better constrain the formation age of the Xitieshan deposit, three samples from the lower Tanjianshan Group in the mine area were selected for U-Pb zircon geochronology. They are rhyolite porphyry (sample XTS16-1 from unit a-1) and clastic sedimentary rocks (sample DC09-1 from unit a-2 and sample DC13-1 from unit b). The locations of the samples are shown in Fig. 2. The analytical method for U-Pb geochronology is outlined in Appendix A. The results of isotopic measurements on zircon (all errors are given at the 1σ level) are listed in Table 1 and are shown in conventional U-Pb concordia plots in Fig. 13.

Sample XTS16-1 rhyolite porphyry (from unit a-1) contained colorless to brownish prismatic zircons with aspect ratio from 1 to 2 and oscillatory magmatic zoning. The ratios of Th/U range from 0.31 to 0.86

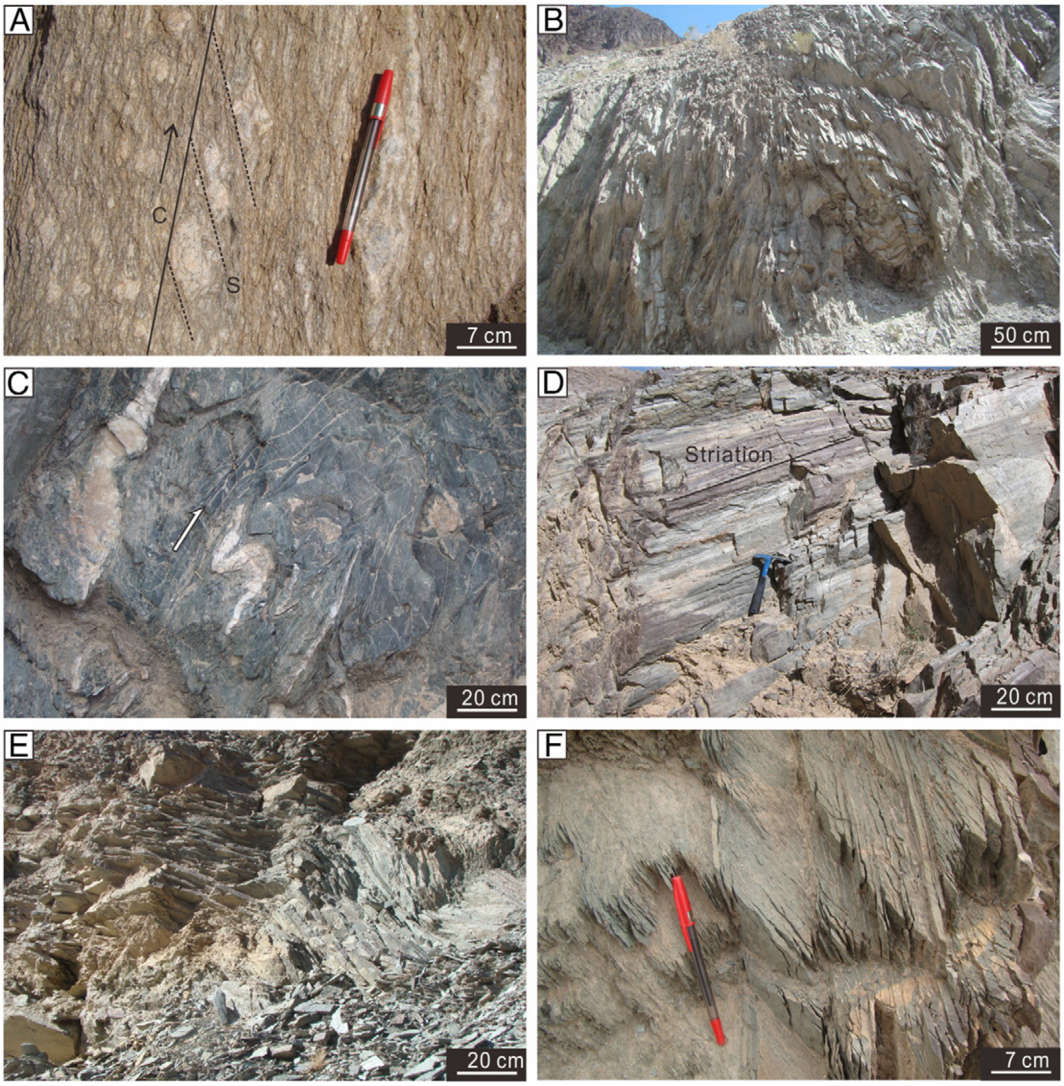

Fig. 9. A. An S-C fabric in granitic gneiss, indicates the dextral shear deformation in the Dakendaban Group. B. The medium-scale folds in unit d-1. C. S- type fold of the calcite vein, indicate the dextral shear deformation, unit d-3. D. Mullion structure and striation on the plane, indicate obliquely thrust extrusion, unit d-1. E. Kink-band structure of the chlorite schist, indicate the dextral shear deformation, unit d-3. F. Two conjugate fracture cleavages in unit d-3.

(Table 1), also characteristic of the magmatic zircon (Möller et al., 2003; Rubatto and Gebauer, 2000). Twenty-five analyses of small single euhedral grains were carried out, and all of them plot on the concordia (Fig. 13A). Their ages range from 450 ± 12 Ma to 456 ± 12 Ma and mutually overlap; the weighted average of these ^{206}Pb/^{238}U ages is 454.1 ± 4.2 Ma (MSWD = 0.02) (Fig. 13B), which define an age of crystallization of rhyolite porphyry in unit a-1.

Sample DC09-1 clastic sedimentary rock (from unit a-2), contained many zircons, most of them colorless to brownish in color and generally prismatic in shape. The ratios of Th/U range from 0.08 to 0.95 (Table 1). Twenty-five selected grains were analyzed and gave concordant data with a wide range of ^{207}Pb/^{206}Pb or ^{206}Pb/^{238}Pb ages (from 452 ± 7 to 1759 ± 74 Ma) (Table 1) (Fig. 13C, D, E, F). With the exception of the five grains that are lower than the 95% confidence level, the major peak value is 917 Ma (Fig. 13D, F), which is the protolith age of granitic gneiss in the Dakendaban Group (Zhang et al., 2009; Zhang et al., 2006), suggesting zircon inheritance. The presence of inherited zircons within the 917 Ma clastic sedimentary rocks that host the Xitieshan deposit strongly suggests that unit a was deposited on an older crust that included ca. 917 Ma components. Furthermore, one inherited Paleoproterozoic zircon (1759 Ma) (Table 1) also suggests the presence of even older basement to the area. The younger age group includes four grains ranging from 452 ± 7 to 453 ± 8 Ma with a mean value of 452 ± 8 Ma (Fig. 13E). This younger age is interpreted to be the maximum age of deposition for unit a-2 volcaniclastic rocks and overlaps the ages for unit a-1.

Sample DC13-1 is a clastic sedimentary rock from unit b, collected in the Duancenggou area. The sample contained colorless to brownish automorphic and prismatic zircons. Thirty grains were analyzed; with the exception of three grains that are lower than the 95% confidence level, the ages range from 451 ± 8 to 3350 ± 14 Ma (Table 1) (Fig. 13G, H). The minimum peak value of the 451 ± 8 Ma was obtained from four grains (Fig. 13I), representing the maximum age for deposition of unit b. The age of other inherited zircons (i.e. 918 Ma) (Fig. 13J) within the clastic sedimentary rocks of unit b suggests their source is mainly from the nearby Dakendaban Group to the northeast.

7.2. Age of the ductile shear deformation

In the Xitieshan area, the main northwest-southeast trending ductile shear zone occurs at the contact between the Dakendaban Group in the basement and the Tanjianshan Group. In order to determine the formation age of the ductile shear zone, we dated muscovite from granitic mylonite in the Xitieshan dextral transpression ductile shear zone.

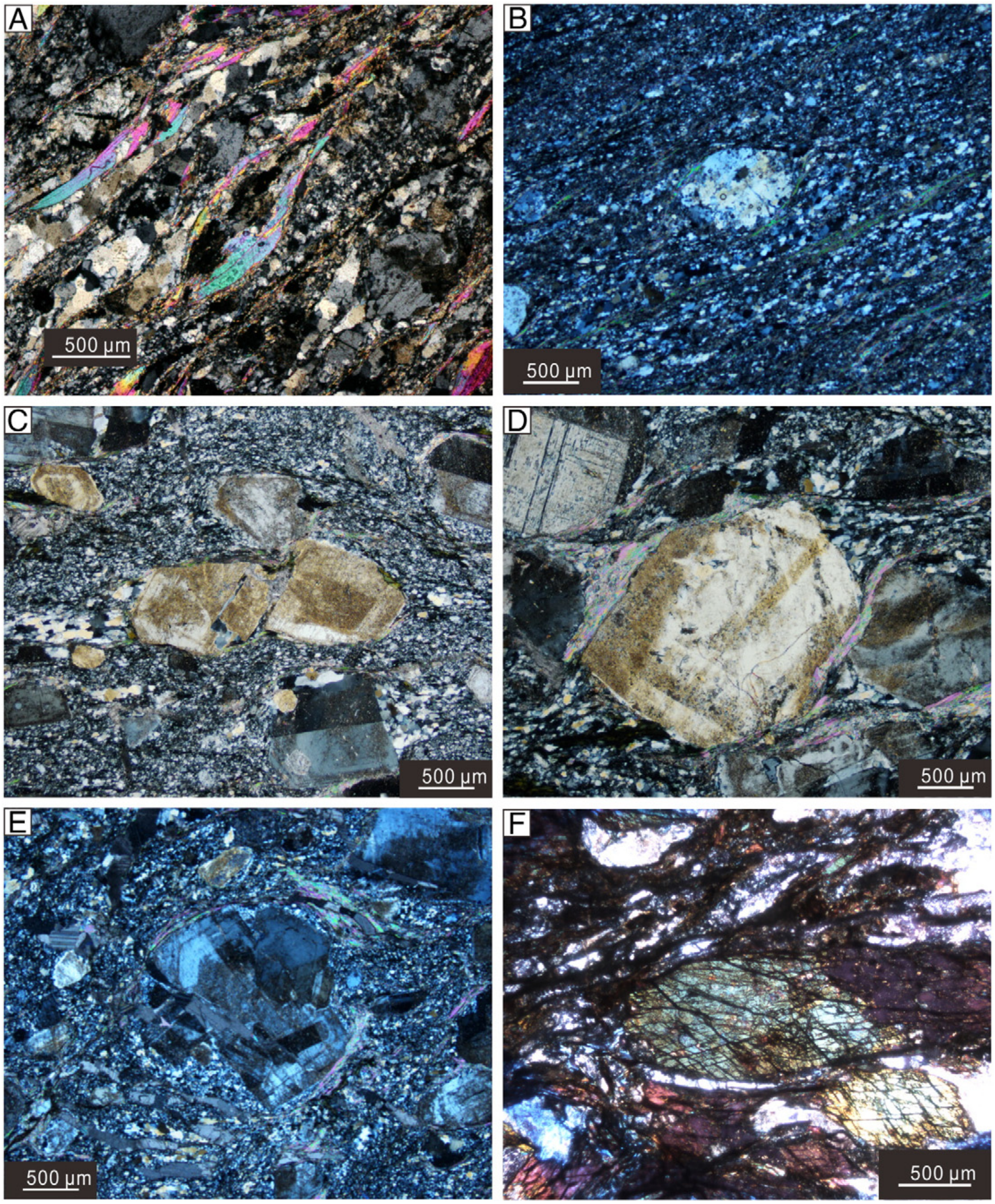

Fig. 10. A. Micrograph showing the kinked and lengthened mica of the mylonitization granitic gneiss in the Dakendaban Group (X-polarized light). B. Micrograph showing strong mylonitization felsic volcanic rocks in unit a-1 (X-polarized light). C. Micrograph showing the snapped feldspar porphyroblast of rhyolite porphyry in unit a-1 (X-polarized light). D. Micrograph showing the δ type feldspar phenocryst of rhyolite porphyry in unit a-1 (X-polarized light). E. Micrograph showing phenocryst rotation structure in unit a-2 (X-polarized light). F. Micrograph showing the lenticular amphibole phenocryst in unit a-1 (X-polarized light).

Sample 10XTS-02 was collected from the mylonitized granitic gneisses of the lower ductile shear zone at the bottom of Zhongjiangou in the Xitieshan area (Fig. 2). The analytical method for ^{40}Ar-^{39}Ar dating is outlined in Appendix A.

The muscovite ages from the mylonitized granitic gneisses (sample 10XTS-02) range from 391 ± 2 Ma to 405 ± 2 Ma, obtained through 20 heating steps (Table 2), and yielded a very good plateau age of 398 ± 4 Ma (Fig. 14A). The inverse isochronal age is 399 ± 4 Ma (Fig. 14B), in good agreement with the plateau age. Given the mylonitized granitic gneisses in the ductile shear zone, the muscovite closure temperature is about 350 ± 50 °C, which explains muscovite growth under the relatively low temperatures (Xu et al., 2006). Therefore, the inverse isochronal age of 399 ± 4 Ma is considered to be the age of mylonitization, which is also the formation age of the dextral ductile shear zone in the Xitieshan area.

8. Discussion

8.1. Timing of VMS mineralization in the Tanjianshan Group

Based on the stratigraphic, mineralogical, geochemical and structural context of the Xitieshan mine area, the Xitieshan deposit has been interpreted to have formed during a period of active felsic volcanism and sedimentation within a back-arc marine basin in Middle to Late Ordovician times along the continental margin (Sun et al., 2012). The presence of the island arc volcanic rocks, carbonaceous schist, carbonate and

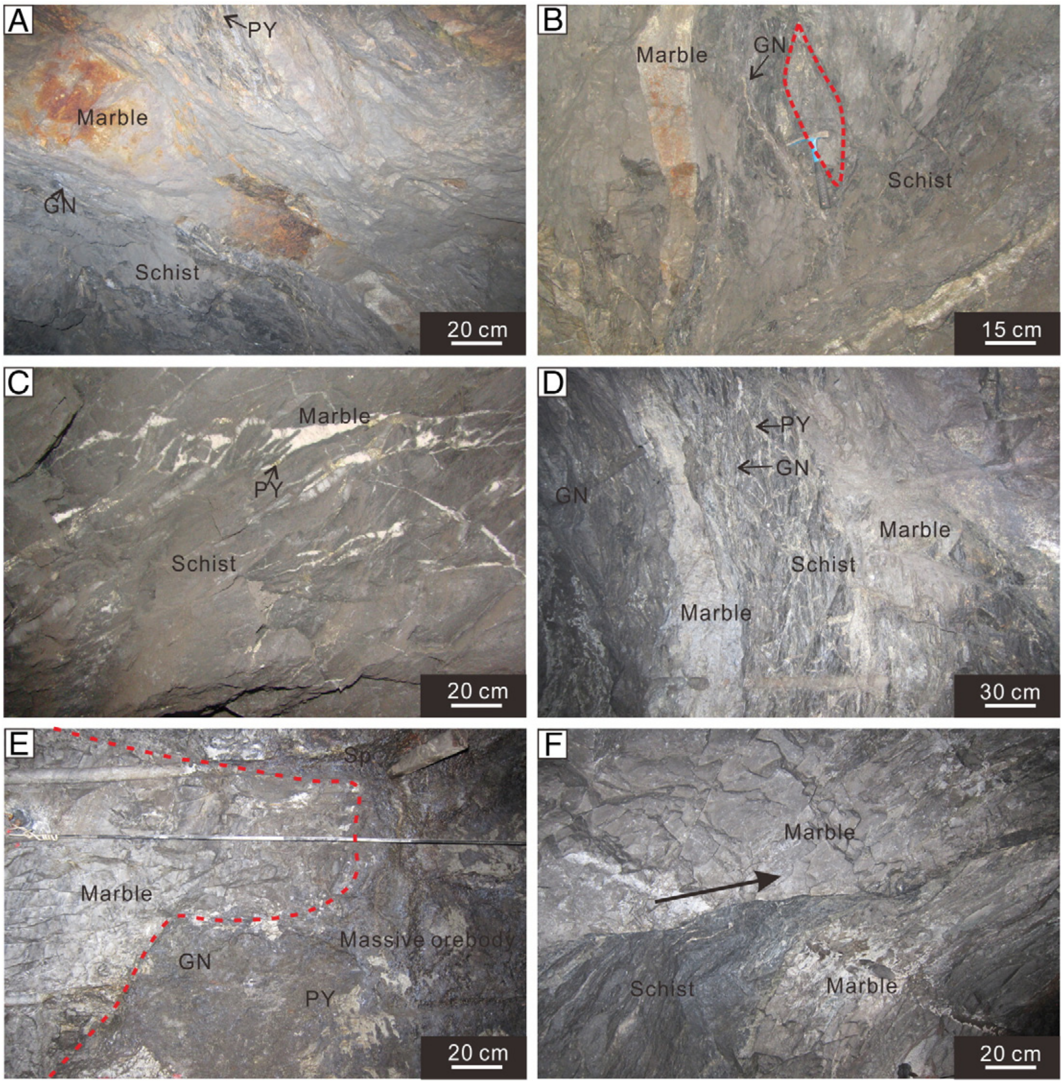

Fig. 11. The underground macrophotographs from the Xitieshan deposit. A. Marble has undergone strong shear deformation at the contact with carbonaceous schist, display a series of lens in different scales, boudinage structure, massive sulfides distribute both the ends of the lens. B. Marble occurs as the form of lens in the carbonaceous schist, the massive sulfides always fill the structure extensional space (the arrow). C. Marble stringer veins with the carbonaceous schist, obviously offset by the late shear deformation, two ends of the stringer veins are filled with the sulfides. D. Marble interlayer with the carbonaceous schist, strong developed foliated, the foliated space was filled the sulfides. E. Massive sulfides distribute in the end of the lens. F. Carbonaceous schist is sandwiched in marble, suffered ductile shear deformation. PY = pyrite, GN = galena, SP = sphalerite.

the VMS deposit suggests that this marine basin formed on the arcward-facing margin of the ensialic back-arc basin between the arc and continental margin.

The formation age of the Tanjianshan Group was debated for a long time. In ca. 1980, the coral (*Favistella* and *Paleadithostrotion* sp.) and brachiopod fossils were found firstly in the marble of the lower Tanjianshan Group (unit a) during the regional mapping, suggesting that the formation age of the Tanjianshan Group is Late Ordovician. Zhao et al. (2003) obtained the single zircon U-Pb age of 483 ± 13 Ma from the felsic volcanic rocks in unit a-1, and further interpreted that they formed in the continental-rift environment during the Early Ordovician. Li et al. (2007) speculated that the Tanjianshan Group formed from 496 to 440 Ma, in the entire Ordovician based on comprehensive analysis of the field geological features, paleontological association, isotope ages and volcanic sedimentary evolution. On the other hand, there are also three genetic types in the Xitieshan deposit: 1) hydrothermal metasomatism (Zhang et al., 1995); 2) volcanogenic massive sulfide deposit (Wu et al., 1987); and 3) SEDEX-type (Zhang et al., 2005). The Xitieshan massive sulfide deposits are hosted by the volcanic sedimentary rocks, in which hydrothermal fluids played an important role, and the Rhenium (Re) content in pyrite is very low, only up to ppb levels. Therefore, both the magmatic zircons from the felsic rhyolite and detrital zircons from sedimentary rocks were analyzed firstly by using U–Pb LA-ICP-MS to help establish the temporal and stratigraphic relationship between volcanism of unit a-1 and sedimentation of unit a-2 and unit b at the early volcanic sedimentary cycle, and further constrain the mineralization of the Xitieshan deposit. Our new isotopic ages from units a and b of the Tanjianshan Group (454 to 451 Ma) are in good agreement with the fossil evidence, suggesting that there are at least two periods of mineralization during the early volcanic sedimentary cycle, and both are in the Late Ordovician.

The timing of felsic volcanism is defined by a concordia age of 454 ± 0.9 Ma (Fig. 13A), which is taken as the primary igneous age of the felsic VMS host rock that resulted from the ocean crust subduction, characterized by the island arc volcanic rocks (Sun et al., 2012). Both sedimentary host rocks of unit a-2 and unit b have maximum ages of ca. 452 Ma and 451 Ma, respectively. The results show that the immediate host rocks formed in Late Ordovician time.

Based on these age data and the assumption that the Xitieshan deposit is of syngenetic nature (VMS or SEDEX), it is proposed that bimodal volcanic rocks formed at ca. 454 Ma, in a back-arc extensional environment associated with plate subduction; the magmatism

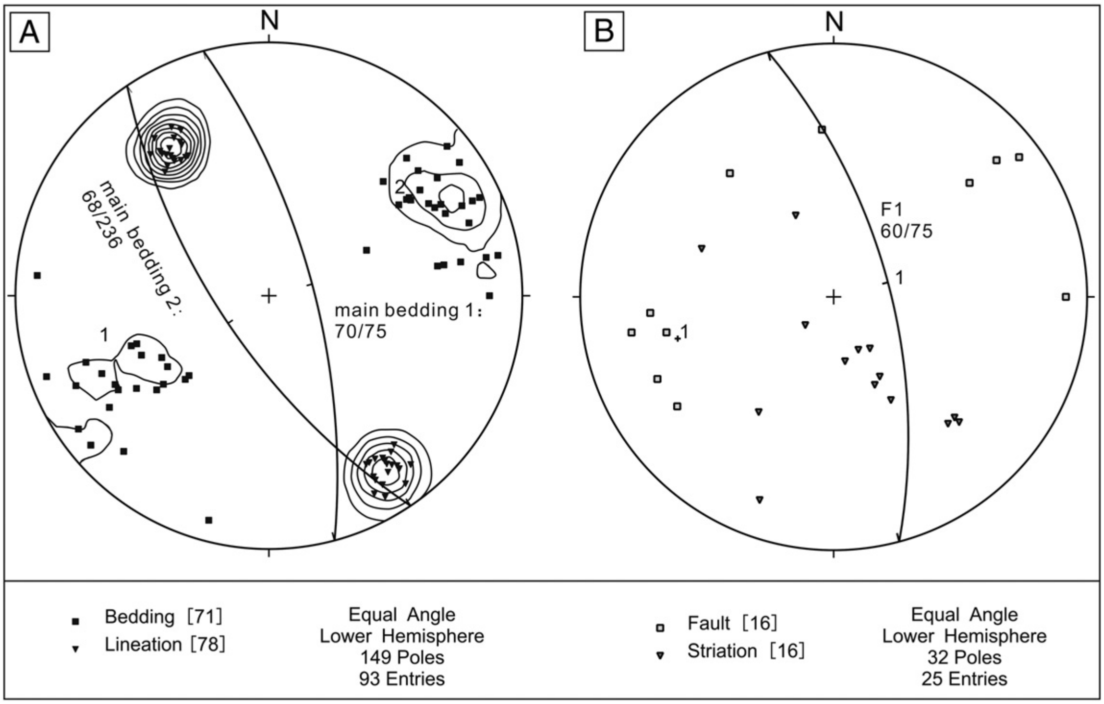

Fig. 12. A. Stereographic projection (Wulff lower hemisphere) of fabrics related to the early ductile deformation event and the bedding. B. Stereographic projection (Wulff lower hemisphere) of fabrics related to the brittle fault.

provided abundant heat and the ore-forming material for the formation of the Xitieshan deposit. From 454 to 452 Ma, felsic magmatism and sedimentation took place simultaneously and in alternation, and hydrothermal mineralization continued. In the local oxygen-deficient basin environment (e.g. abundant black carbonaceous schist), the carbonaceous schist and carbonate resulted from the sedimentation, and became the best host rocks for the Xitieshan mineralization. Subsequently, at about 451 Ma, volcanism weakened, whereas sedimentation continued and strengthened, and hydrothermal activities were manifested by the development of the iron-manganese carbonate horizon, as well as minor exhalative deposits in unit b.

Therefore, the formation ages of unit a-2 and unit b are the best estimate for the relative age of mineralization in the Xitieshan district, as VMS hydrothermal systems are commonly synchronous with the volcanism that produced their host rocks, or nearly so (Barrie and Hannington, 1999). The main mineralizing events followed the eruption and deposition of unit a-1 silicic magmas and are synchronous with sedimentation of unit a-2 and unit b at the onset of back-arc volcanism.

8.2. Relationship between the deposit and the ductile shear zone

The formation age of the Tanjianshan Group in North Qaidam ranges from 514 Ma to 440 Ma, overall belonging to the Late Cambrian-Ordovician (Li et al., 2007; Shi et al., 2006; Zhao et al., 2003), and predominantly concentrating at ca. 450 Ma in the Xitieshan area from the above discussion. ^{40}Ar-^{39}Ar age for muscovite from the mylonitized granitic gneisses in the ductile shear zone is ~399 Ma, which represents the formation age of the Xitieshan ductile shear zone, suggesting that metamorphism and deformation post-dated the Tanjianshan Group and is Early Devonian in age.

The major ore-bearing stratum at the bottom of the Tanjianshan Group (units a and b) in the Xitieshan mining area is close to the ductile shear zone (Fig. 2), and is characterized by strong shear-compression deformation, well-developed schistosity and medium-grade metamorphism. The massive sulfide deposit is hosted by the metasedimentary rocks that mainly include the marble, schist and transitional zone between the marble and schist (Fig. 4), corresponding to three types of the deposits, marble-hosted, schist-hosted, and transitional-hosted, respectively (Zhang et al., 2005).

Based on the field observations (Fig. 11) and drill hole data (Fig. 4), the ore-bearing strata have been broken into the two parts during the later ductile shear deformation: one is the greenschist facies, incompetent rocks which experienced strong ductile deformation, and the another is the tectonic lens of marble, competent rocks which undergone relatively weak shear deformation (Figs. 4, 11) (Wang et al., 2000). Both ends of the structural lens of the marble experienced the strongest compressional deformation. Different deformation fields resulted in the different scales, shapes and types of orebodies (Figs. 4, 11). In the strong deformation zones, the deformation is characterized by the complete structural replacement function and high homogenization. Both the marble and orebodies were elongated due to the strong shearing action, became thinner, and basically parallel with the mylonite foliation (Fig. 11A). The orebodies have small thickness, discontinuous distribution, low grade, and its morphology is relatively consistent (Fig. 11B, C and D). However, within the weak deformation zones, the deformation is characterized by incomplete structural transposition, lesser homogenization, and primary controlling structures of the orebodies are well preserved (Fig. 11E, F). The massive sulfide ore bodies that are hosted in the marble of the weak deformation reveal large thickness, good continuity, high grade, and the forms of the orebodies are variable. Marble is characterized by variation in size, and formed a series of overlapping tectonic lens. The Xitieshan deposit was modified during deformation, and predominantly hosted in the tension crack of the marble tectonic lenses and structural collapse transitional zone between the marble and greenschist (Fig. 4). In addition, the inclined column type distribution of the orebodies, the presence of the complex fold and the expansion of the massive orebodies that were thinned, abrupt and offset by the fault in the structural extension zone (Fig. 4), these appearances are caused by the late tectonic movement. Therefore, it is obvious that the Xitieshan deposit was controlled by the post-mineral deformation.

Table. 1
LA-ICPMS U-Pb analytical data for magmatic zircons in sample XTS16-1, detrital zircons in sample DC09-1 and DC13-1.

Sample	Pb^T	^{232}Th	^{238}U	Th/U	$^{207}Pb/^{206}Pb$		$^{207}Pb/^{235}U$		$^{206}Pb/^{238}U$		$^{207}Pb/^{206}Pb$		$^{207}Pb/^{235}U$		$^{206}Pb/^{238}U$		Concor-dance
Date spot	(ppm)	(ppm)	(ppm)		Ratio	1σ	Ratio	1σ	Ratio	1σ	Age (Ma)	1σ	Age (Ma)	1σ	Age (Ma)	1σ	
Sample XTS16-1																	
XTS16-101	12.0	101	137	0.74	0.05736	0.0036	0.57684	0.0397	0.07246	0.0021	505.6	137.0	462.4	25.6	450.9	12.3	97%
XTS16-102	21.5	149	249	0.60	0.05533	0.0035	0.55538	0.0300	0.07255	0.0023	433.4	140.7	448.5	19.6	451.5	13.8	99%
XTS16-103	10.9	77	128	0.60	0.05753	0.0039	0.57086	0.0362	0.07311	0.0020	522.3	143.5	458.6	23.4	454.9	12.0	99%
XTS16-104	13.7	71	173	0.41	0.05559	0.0050	0.55187	0.0458	0.07324	0.0018	435.2	200.0	446.2	29.9	455.6	10.9	97%
XTS16-105	32.3	263	378	0.70	0.05578	0.0031	0.56210	0.0296	0.07309	0.0015	442.6	122.2	452.9	19.2	454.7	9.1	99%
XTS16-106	9.2	39	124	0.31	0.05796	0.0052	0.56055	0.0482	0.07266	0.0028	527.8	202.8	451.9	31.3	452.1	16.9	99%
XTS16-107	27.0	237	302	0.78	0.05610	0.0034	0.56866	0.0329	0.07317	0.0017	457.5	133.3	457.1	21.3	455.2	10.1	99%
XTS16-108	16.5	119	195	0.61	0.05592	0.0035	0.57123	0.0375	0.07321	0.0016	450.0	138.9	458.8	24.2	455.5	9.8	99%
XTS16-109	12.4	79	151	0.52	0.05818	0.0041	0.58979	0.0393	0.07279	0.0018	600.0	155.5	470.7	25.1	453.0	11.0	96%
XTS16-110	19.5	129	235	0.55	0.05608	0.0042	0.57045	0.0396	0.07289	0.0018	453.8	166.6	458.3	25.6	453.5	10.9	98%
XTS16-111	18.5	131	216	0.61	0.05520	0.0035	0.56629	0.0340	0.07318	0.0018	420.4	140.7	455.6	22.0	455.3	10.6	99%
XTS16-112	14.6	143	166	0.86	0.05701	0.0034	0.58250	0.0351	0.07292	0.0018	500.0	131.5	466.1	22.5	453.7	10.9	97%
XTS16-113	27.0	209	319	0.65	0.05557	0.0029	0.57765	0.0306	0.07323	0.0016	435.2	112.0	463.0	19.7	455.6	9.7	98%
XTS16-114	18.2	106	226	0.47	0.05761	0.0037	0.59620	0.0378	0.07322	0.0016	522.3	140.7	474.8	24.1	455.5	9.5	95%
XTS16-115	13.7	94	167	0.56	0.05372	0.0039	0.55258	0.0405	0.07311	0.0020	366.7	164.8	446.7	26.5	454.9	12.1	98%
XTS16-116	12.4	70	157	0.45	0.05683	0.0042	0.59116	0.0444	0.07321	0.0020	483.4	158.3	471.6	28.3	455.4	11.7	96%
XTS16-117	13.5	66	170	0.39	0.05754	0.0040	0.58543	0.0386	0.07341	0.0020	522.3	151.8	467.9	24.7	456.6	12.3	97%
XTS16-118	12.0	90	142	0.63	0.05789	0.0062	0.59927	0.0668	0.07308	0.0017	524.1	237.0	476.8	42.4	454.7	10.5	95%
XTS16-119	27.5	161	337	0.48	0.05640	0.0032	0.57847	0.0314	0.07279	0.0015	477.8	123.1	463.5	20.2	452.9	8.9	97%
XTS16-120	10.4	70	125	0.56	0.05463	0.0052	0.55099	0.0514	0.07267	0.0025	398.2	214.8	445.6	33.7	452.2	14.9	98%
XTS16-121	10.2	86	114	0.75	0.05727	0.0054	0.58964	0.0623	0.07236	0.0025	501.9	209.2	470.6	39.8	450.3	15.0	95%
XTS16-122	36.7	202	442	0.46	0.05495	0.0034	0.56169	0.0356	0.07264	0.0014	409.3	138.9	452.6	23.2	452.1	8.6	99%
XTS16-123	13.1	76	157	0.48	0.05594	0.0035	0.57061	0.0353	0.07300	0.0016	450.0	138.9	458.4	22.8	454.2	9.5	99%
XTS16-124	24.2	166	291	0.57	0.05668	0.0032	0.58158	0.0341	0.07301	0.0017	479.7	124.1	465.5	21.9	454.2	10.0	97%
XTS16-125	13.8	69	171	0.41	0.05710	0.0039	0.57056	0.0380	0.07269	0.0018	494.5	150.0	458.4	24.6	452.4	10.6	98%
Sample DC09-1																	
DC09-112	34.1	193	428	0.45	0.05494	0.0024	0.55453	0.0242	0.07257	0.0012	409.3	98.1	448.0	15.8	451.6	7.3	99%
DC09-109	25.8	151	317	0.47	0.05240	0.0025	0.53246	0.0254	0.07264	0.0016	301.9	107.4	433.4	16.9	452.0	9.3	95%
DC09-105	16.7	96	208	0.46	0.05447	0.0027	0.54984	0.0275	0.07276	0.0018	390.8	111.1	444.9	18.0	452.8	10.7	98%
DC09-125	26.4	151	327	0.46	0.05508	0.0024	0.55096	0.0244	0.07277	0.0014	416.7	100.0	445.6	16.0	452.8	8.4	98%
DC09-106	42.1	101	569	0.18	0.05503	0.0026	0.55931	0.0282	0.07290	0.0020	413.0	108.3	451.1	18.4	453.6	11.9	99%
DC09-114	41.0	153	236	0.65	0.06903	0.0025	1.41284	0.0529	0.14749	0.0023	899.7	69.4	894.4	22.3	886.9	12.7	99%
DC09-107	91.2	63	592	0.11	0.06558	0.0025	1.39740	0.0515	0.15259	0.0023	794.4	81.5	887.8	21.8	915.5	12.9	96%
DC09-103	107.4	77	738	0.10	0.06708	0.0021	1.42131	0.0476	0.15272	0.0029	840.4	65.9	897.9	19.9	916.2	16.4	97%
DC09-123	104.8	102	692	0.15	0.06895	0.0022	1.45782	0.0477	0.15281	0.0020	898.2	65.9	913.1	19.7	916.7	11.3	99%
DC09-102	81.8	55	547	0.10	0.06889	0.0022	1.46264	0.0523	0.15283	0.0027	894.4	66.7	915.1	21.6	916.8	15.2	99%
DC09-113	98.6	69	651	0.11	0.06637	0.0021	1.41000	0.0459	0.15295	0.0024	818.2	63.7	893.2	19.3	917.5	13.7	97%
DC09-119	75.3	53	509	0.10	0.06719	0.0024	1.42093	0.0567	0.15296	0.0036	842.6	74.1	897.8	23.8	917.6	20.0	97%
DC09-121	87.6	460	483	0.95	0.06924	0.0032	1.46629	0.0748	0.15298	0.0038	905.6	95.5	916.6	30.8	917.6	21.1	99%
DC09-118	77.2	70	502	0.14	0.06707	0.0022	1.41962	0.0483	0.15306	0.0023	838.9	69.3	897.2	20.3	918.1	12.9	97%
DC09-101	76.6	66	503	0.13	0.07264	0.0026	1.54300	0.0573	0.15309	0.0024	1005.6	71.1	947.7	22.9	918.3	13.2	96%
DC09-111	96.0	83	635	0.13	0.06819	0.0025	1.45744	0.0525	0.15318	0.0023	875.9	74.1	913.0	21.7	918.8	13.1	99%
DC09-120	103.4	73	698	0.10	0.06649	0.0027	1.41186	0.0609	0.15323	0.0030	821.9	80.6	893.9	25.6	919.1	16.9	97%
DC09-117	82.3	50	552	0.09	0.06690	0.0021	1.41855	0.0505	0.15324	0.0028	835.2	65.3	896.8	21.2	919.1	15.9	97%
DC09-104	78.8	45	534	0.08	0.06699	0.0025	1.42767	0.0559	0.15327	0.0032	838.9	81.6	900.6	23.4	919.3	17.9	97%
DC09-116	12.7	25	36	0.69	0.10759	0.0044	4.61544	0.2015	0.31128	0.0061	1759.0	74.2	1752.1	36.4	1747.0	29.9	99%
Sample DC13-1																	
DC13-116	36.0	370	386	0.96	0.05708	0.0023	0.57316	0.0245	0.07247	0.0013	494.5	58.3	460.1	15.8	451.0	7.8	98%
DC13-117	54.3	633	554	1.14	0.05823	0.0017	0.58498	0.0178	0.07249	0.0010	538.9	69.4	467.7	11.4	451.2	5.8	96%
DC13-102	56.9	604	616	0.98	0.06126	0.0028	0.58185	0.0335	0.07255	0.0018	650.0	98.1	465.6	21.5	451.5	10.8	96%
DC13-126	34.5	402	418	0.96	0.05841	0.0027	0.58987	0.0255	0.07270	0.0014	546.3	100.0	470.8	16.3	452.4	8.5	96%
DC13-122	31.6	266	285	0.94	0.06225	0.0028	0.77403	0.0320	0.08972	0.0018	683.3	96.3	582.1	18.3	553.9	10.7	95%
DC13-108	48.18	34.7	519	0.07	0.05859	0.0017	0.77819	0.0253	0.09539	0.0017	553.7	63.0	584.4	14.5	587.3	10.2	99%
DC13-113	23.21	221	149	1.48	0.06540	0.0032	1.08532	0.0542	0.12055	0.0026	787.0	103.7	746.2	26.4	733.7	15.2	98%
DC13-110	26.3	236	149	1.58	0.06495	0.0022	1.07984	0.0346	0.12070	0.0020	772.2	71.4	743.6	16.9	734.6	11.3	98%
DC13-105	51.0	683	309	2.21	0.06770	0.0031	1.14057	0.0474	0.12110	0.0021	861.1	95.2	772.8	22.5	736.9	12.3	95%
DC13-109	23.00	112	121	0.93	0.07357	0.0033	1.53356	0.0531	0.15301	0.0031	1031.5	90.0	943.9	21.3	917.8	17.1	97%
DC13-120	40.9	246	193	1.27	0.07410	0.0029	1.57554	0.0586	0.15308	0.0025	1044.1	77.8	960.6	23.1	918.2	14.2	95%
DC13-115	45.1	119	254	0.47	0.07423	0.0017	1.56893	0.0403	0.15312	0.0020	1047.8	47.4	958.0	15.9	918.4	11.0	95%
DC13-118	91.1	381	483	0.79	0.07451	0.0018	1.58509	0.0431	0.15313	0.0022	1055.3	48.6	964.4	16.9	918.5	12.6	95%
DC13-112	20.7	139	92.0	1.51	0.07505	0.0027	1.57154	0.0504	0.15325	0.0022	1070.1	70.4	959.0	19.9	919.2	12.4	95%
DC13-124	54.7	185	260	0.71	0.07899	0.0054	2.02816	0.1482	0.18515	0.0035	1172.2	136.4	1125.0	49.7	1095.1	19.2	97%
DC13-101	97.12	95.2	527	0.18	0.07863	0.0028	2.02992	0.0816	0.18551	0.0034	1162.7	66.5	1125.6	27.3	1097.0	18.5	97%
DC13-129	41.6	106	207	0.51	0.07549	0.0032	1.93720	0.0876	0.18578	0.0046	1083.3	85.2	1094.0	30.3	1098.5	24.8	99%
DC13-106	67.3	111	342	0.32	0.08107	0.0031	2.11364	0.0857	0.18596	0.0035	1233.3	75.9	1153.3	28.0	1099.5	19.2	95%
DC13-127	51.0	188	225	0.84	0.07915	0.0030	2.12762	0.0756	0.19361	0.0031	1175.9	75.2	1157.8	24.5	1140.9	16.9	98%
DC13-125	54.6	160	186	0.86	0.09779	0.0040	3.52304	0.1436	0.25850	0.0063	1583.3	75.9	1532.4	32.3	1482.2	32.5	96%
DC13-107	95.2	275	316	0.87	0.09769	0.0030	3.52406	0.1059	0.25863	0.0035	1580.6	57.4	1532.6	23.8	1482.8	17.8	96%
DC13-128	119.5	153	346	0.44	0.11929	0.0037	5.41206	0.1769	0.32635	0.0057	1946.3	49.8	1886.8	28.0	1820.7	27.5	96%
DC13-130	114.6	67.8	282	0.24	0.14194	0.0048	8.09051	0.3265	0.41298	0.0102	2250.9	58.8	2241.2	36.5	2228.5	46.7	99%

(continued on next page)

Table. 1 (*continued*)

Sample	Pb^T	^{232}Th	^{238}U	Th/U	$^{207}Pb/^{206}Pb$		$^{207}Pb/^{235}U$		$^{206}Pb/^{238}U$		$^{207}Pb/^{206}Pb$		$^{207}Pb/^{235}U$		$^{206}Pb/^{238}U$		Concor-dance
Date spot	(ppm)	(ppm)	(ppm)		Ratio	1σ	Ratio	1σ	Ratio	1σ	Age (Ma)	1σ	Age (Ma)	1σ	Age (Ma)	1σ	
DC13-119	221.4	316	378	0.83	0.18598	0.0048	12.41261	0.3569	0.47962	0.0084	2707.1	43.1	2636.1	27.0	2525.6	36.7	95%
DC13-123	134.0	152	258	0.59	0.17247	0.0054	11.71758	0.4038	0.48548	0.0098	2583.3	53.6	2582.1	32.3	2551.1	42.7	98%
DC13-103	257.2	328	503	0.65	0.17932	0.0053	12.48581	0.4196	0.49844	0.0092	2646.6	48.3	2641.7	31.6	2607.1	39.4	98%
DC13-114	103.3	147	128	1.14	0.27746	0.0024	23.63245	0.3290	0.61729	0.0078	3350.0	13.6	3253.4	13.6	3099.1	31.3	95%

8.3. Analogues to the Xitieshan district

The Xitieshan deposit exhibits many key geological and geochemical features, including 1) a combination of sedimentary and volcanic rocks indicating a back-arc environment along the passive continental margin during the Middle Ordovician; 2) carbonates and carbonaceous schist as major host rocks suggesting an anoxic shallow water environment; 3) typical bimodal volcanic rocks underlying the massive sulfides deposit; 4) base metal-rich ore (Zn + Pb >10%), with minor Ag and Au; 5) the presence of MORB-like volcanic rocks after the main metallogenic period (Sun et al., 2012); 6) the presence of the multilayer iron formations; 7) δ^{34}S values ranging from 0.8 to 5.4 per mil, and high fluid salinities (12–18 wt.% NaCl equiv.) (Wang et al., 2009; Zhu et al., 2010); and 8) the presence of inherited zircons from the host rocks, suggesting that they formed on continental crust.

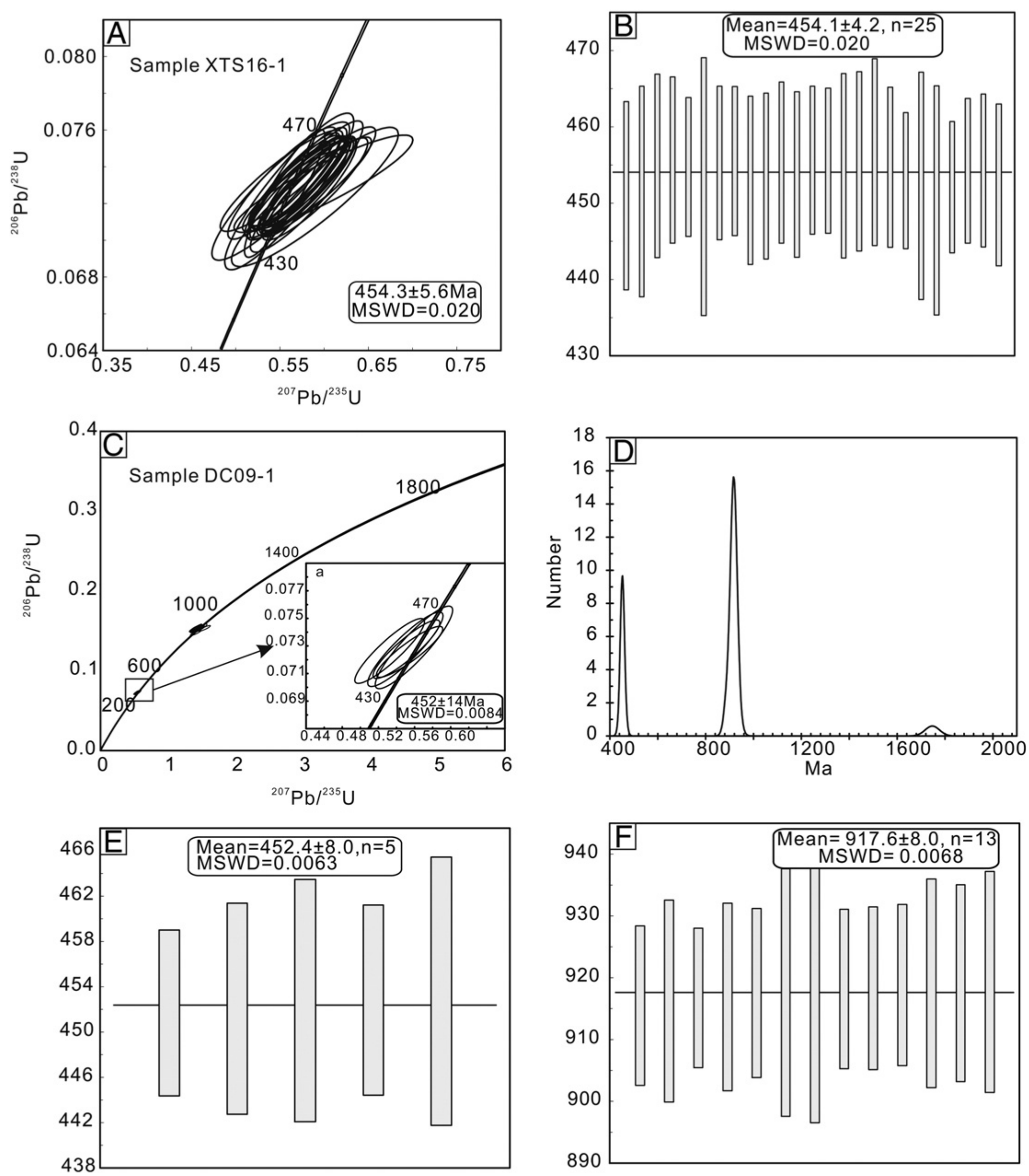

Fig. 13. A and B. U-Pb concordia diagram and weighted average plot for sample XTS16-1, respectively. C and D. U-Pb concordia diagram and probability density plot for sample DC09-1, respectively. E and F. Weighted average plots of the detrital zircons for sample DC09-1. G and H. U-Pb concordia diagram and probability density plot for sample DC13-1, respectively. I and J. weighted average plots of the detrital zircons for sample DC13-1.

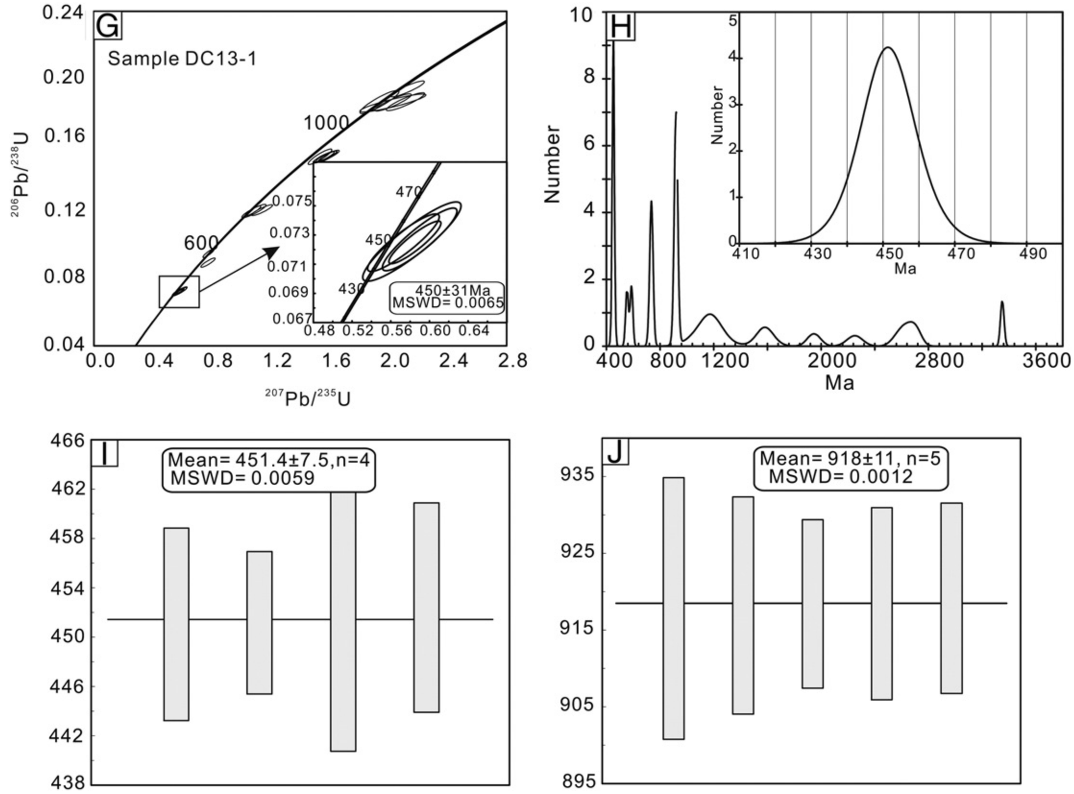

Fig. 13 (*continued*).

A better understanding of the genesis and setting of the Xitieshan deposits, is often aided by their comparison to similar ancient districts (Herzig and Hannington, 1995). The Xitieshan district has many features similar to the Bathurst district of Canada, the Iberian Pyrite Belt of Spain, and the Wolverine volcanogenic massive sulfide deposit in Canada (Fig. 15).

The Ordovician Bathurst Mining Camp (BMC) in Canada, especially the Brunswick 12 deposit, is the best ancient analogue to the Xitieshan district in terms of stratigraphy and geodynamic setting (Fig. 15). The BMC consists of Cambro-Ordovician clastic sedimentary sequence (Miramichi Group) that is characterized by continentally derived flysch facies on a passive continental margin, and Middle Ordovician bimodal volcanic and metasedimentary rocks of the Tetagouche Group that formed during the initial stages of Ordovician rifting behind an ensialic arc (Goodfellow and Peter, 1996; Lentz, 1999; Lentz and McCutcheon, 2006; Mireku and Stanley, 2006; Peter and Goodfellow, 1996; Staal et al., 1991; van Staal et al., 1992). The Tetagouche Group is made up of two packages of felsic volcanic and sedimentary rocks, Nepisiguit Falls and Flat Landing Brook Formation from base to top, respectively (Staal et al., 1991; van Staal et al., 1992), and hosts the majority of the BMC massive sulfide deposits, including the super-giant Brunswick No. 12 and 6 deposits, the Mount Fronsac North deposit, the Camelback Zn-Pb-Cu deposit, the Au-rich Louvicourt deposit, the Flat Landing Brook Zn-Pb-Ag deposit (Goodfellow and Peter, 1996; Lentz, 1999;

Table 2
Dating analyzing results of ^{40}Ar/^{39}Ar.

Steps	Laser energy (%)	^{36}Ar(a)	^{37}Ar(ca)	^{38}Ar(cl)	^{39}Ar(k)	^{40}Ar(r)	Age(Ma)	±2σ	^{40}Ar(r) (%)	^{39}Ar (k) (%)
1	4.5%	0.000157	0.000001	0.000003	0.010540	0.220777	398	2	82.6	0.95
2	4.8%	0.000180	0.000001	0.000006	0.013343	0.273815	391	2	83.7	1.20
3	5.1%	0.000028	0.000004	0.000003	0.005332	0.113992	405	2	93.1	0.48
4	5.5%	0.000117	0.000001	0.000005	0.021896	0.452725	393	2	92.9	1.97
5	5.8%	0.000066	0.000006	0.000004	0.013769	0.288596	398	2	93.7	1.24
6	6.1%	0.000079	0.000003	0.000004	0.020457	0.426536	396	2	94.8	1.84
7	6.5%	0.000091	0.000006	0.000003	0.024739	0.511572	394	2	95.0	2.23
8	6.8%	0.000083	0.000006	0.000005	0.027442	0.569831	395	2	95.8	2.47
9	7.3%	0.000101	0.000005	0.000014	0.042632	0.884273	395	2	96.7	3.84
10	7.6%	0.000111	0.000005	0.000004	0.045158	0.945407	398	2	96.6	4.07
11	7.9%	0.000097	0.000004	0.000002	0.044558	0.932221	398	1	97.0	4.01
12	8.5%	0.000090	0.000009	0.000001	0.053292	1.116415	398	1	97.7	4.80
13	9.0%	0.000123	0.000001	0.000015	0.063557	1.333222	399	1	97.3	5.73
14	9.6%	0.000107	0.000020	0.000008	0.050478	1.057574	398	1	97.1	4.55
15	10.6%	0.000199	0.000012	0.000020	0.136184	2.854032	398	1	98.0	12.27
16	11.6%	0.000225	0.000012	0.000014	0.136182	2.854894	398	1	97.7	12.27
17	13.6%	0.000226	0.000012	0.000021	0.151486	3.177371	399	1	97.9	13.65
18	14.6%	0.000159	0.000033	0.000036	0.114802	2.413756	399	1	98.1	10.34
19	15.6%	0.000102	0.000008	0.000002	0.089138	1.875358	400	1	98.4	8.03
20	17.6%	0.000047	0.000013	0.000006	0.044851	0.945340	400	1	98.5	4.04

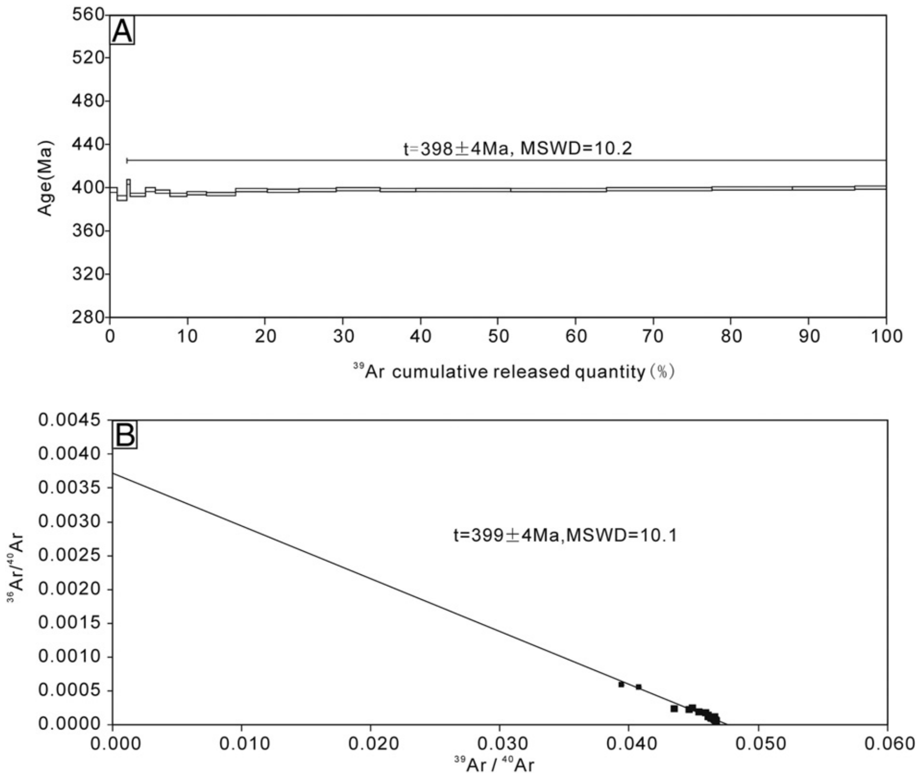

Fig. 14. Age spectrum (A) and isochron plot (B) of muscovite $^{40}Ar/^{39}Ar$ in the sample 10XTS-02.

McclLenaghan et al., 2006; Walker and Carroll, 2006; Walker and Graves, 2006; Walker and Lentz, 2006). Based on the geochemical characteristics, felsic volcanic rocks from both Bathurst and Xitieshan have similar HFSE-REE systematics (Downey et al., 2006; MacLellan et al., 2006; Mireku and Stanley, 2006; Sun et al., 2012; Wills et al., 2006), and they are interpreted to have similar petrogenetic origins and to have formed in a similar tectonic setting.

The Wolverine area of Finlayson Lake district (Yukon, Canada) also exhibits some strong similarities to the Xitieshan area. First of all, both of them have similar host stratigraphic assemblages consisting of volcanic sedimentary rocks, the Wolverine Lake Group vs. the Tanjianshan Group (Fig. 15), which have been interpreted to represent a continental back-arc rift or back-arc basin assemblage (Bradshaw et al., 2008; Bradshaw et al., 2001; Piercey, 2010; Piercey, 2011; Piercey et al., 2002; Piercey et al., 2004; Piercey et al., 2001; Piercey et al., 2008; Wu et al., 2010). The Wolverine succession consists predominantly of felsic volcanic and carbonaceous sedimentary rocks, which host the Wolverine VHMS deposit (6.2 Mt @ 12.96% Zn, 1.53% Pb, 1.41% Cu, 359.1 g/t Ag, 1.81 g/t Au) (Bradshaw, 2003; Bradshaw et al., 2008; Murphy, 1997; Murphy et al., 2006; Piercey et al., 2001; Piercey et al., 2008). The Wolverine deposit occurs at the contact between footwall felsic volcaniclastic rocks and either hanging-wall carbonaceous argillite or exhalative rocks (Bradshaw, 2003). Other similarities between the Xitieshan deposit and the Wolverine deposit (Fig. 15) include the location of the felsic volcanic rocks and massive sulfides deposits, metal grades, the abundance of carbonaceous rocks and volcaniclastic rocks in the host stratigraphy, and the presence of iron formation. Geochemical features suggest that felsic volcanic rocks in the Wolverine Lake district were the products of high-temperature melting of continental crust due to slab roll back and generation of an intracontinental back-arc basin (Murphy et al., 2006; Piercey et al., 2003; Piercey et al., 2001; Piercey et al., 2008). A similar petrogenetic origin and geodynamic setting is proposed for the VMS-related felsic volcanic rocks of the Xitieshan district (Sun et al., 2012; Wu et al., 2010).

Another analogue of the Xitieshan district is the Iberian Pyrite Belt (IPB) of Spain. The IPB contains a lower sequence, the Phyllite-Quartzite (PQ) Group of meta-sedimentary rocks, which is disconformably overlain by the Volcanic Sedimentary Complex (VSC), which hosts the mineralization within the IPB (Fig. 15) (de Oliveira et al., 2011; Leistel et al., 1997; Mitjavila et al., 1997; Relvas et al., 2006a; Sáez et al., 1999; Soriano and Marti, 1999; Tornos, 2006; Tornos et al., 2008). The VSC includes a complex mafic-felsic volcanic sequence interbedded with mudstone and some chemical sedimentary rocks. The massive sulfide deposits are hosted by the felsic volcanic units and/or black schist. The thick layers of chert can either directly cap the massive sulfides or are separated from them by several meters of schist (Tornos, 2006). Key similarities between both mining areas are: 1) the presence of spatially associated and laterally extensive iron formation; 2) the presence of iron- and manganese-rich siliceous exhalites and carbonate-rich chemical sediments at several stratigraphic positions; 3) δ^{34} S compositions of sulfides (ranging from −5.5 to +4.7 per mil in Feitais massive sulfide deposit) (Inverno et al., 2008); 4) the mineralizing fluid from the mixing of a deep, reduced fluid of possible magmatic origin with unmodified seawater (Relvas et al., 2006b; Sánchez-España et al., 2000; Thiéblemont et al., 1997; Wang et al., 2009). Both carbonate-rich ores are interpreted to be biogenic mounds formed close to the hydrothermal vents, which show evidence of formation on an oxic sea floor and reflect the prominent low-temperature (ca. 200 °C) (Relvas et al., 2006b) hydrothermal activity.

Based on the above analogical comparisons, combined with five key characteristics of VSHMS-type deposits from the Wolverine deposit (Bradshaw et al., 2008) and other previous researches (Barrie and Hannington, 1999; Goodfellow and McCutcheon, 2003; Sáez et al., 1999), the Xitieshan deposit is very similar to VSHMS deposits in sediment back-arc continental rifting basins compared with the Bathurst Mining Camp, Finlayson Lake, and Iberian Pyrite Belt (Bradshaw et al., 2008; Goodfellow, 2002; Goodfellow and Lydon, 2007; Wills et al., 2006). It is therefore reasonable that the Xitieshan deposit should be ascribed to the VSHMS deposits.

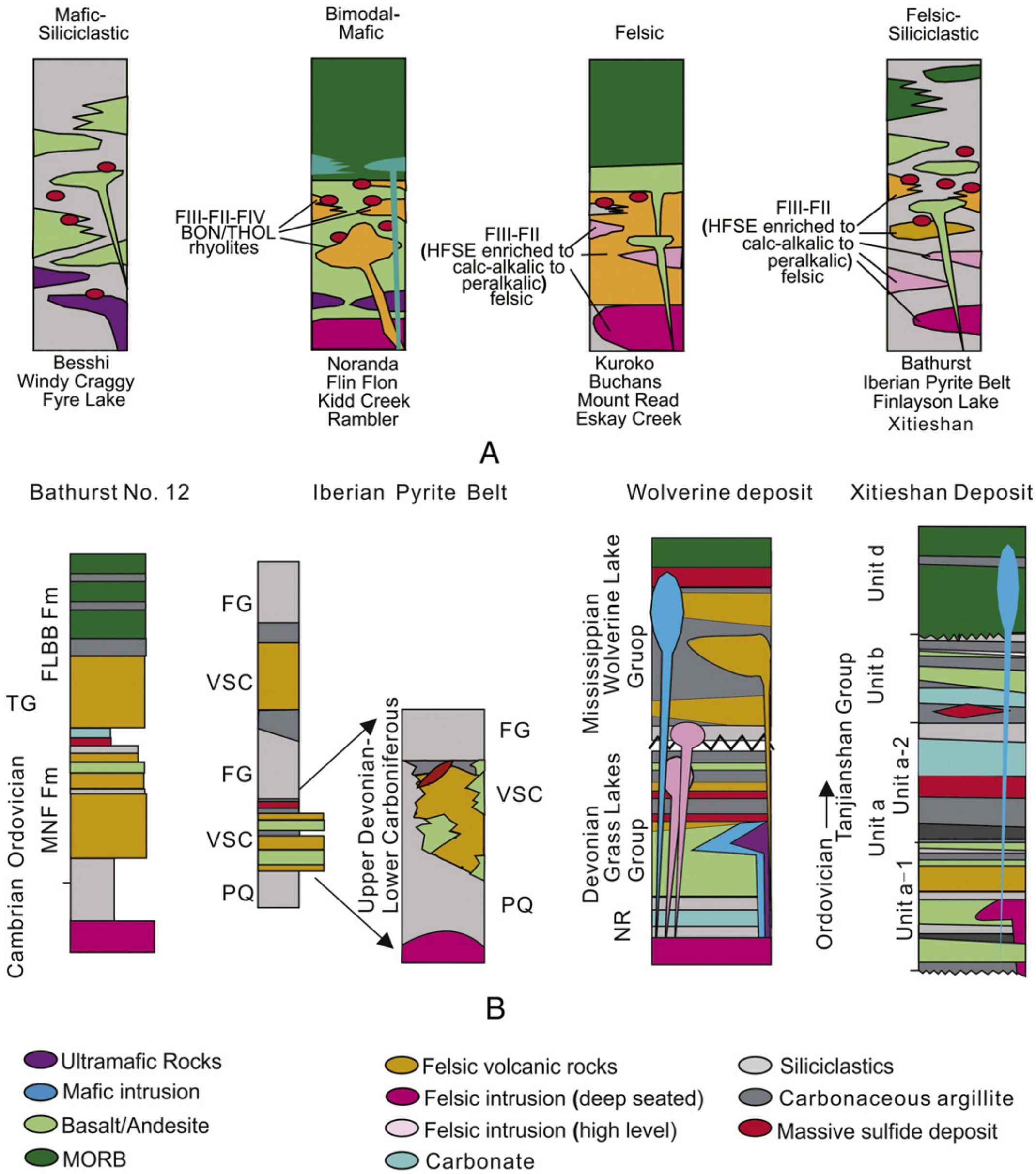

Fig. 15. A. Stratigraphic relationships and potential chemostratigraphic associations for four different VMS deposit groups. Map modified from Piercey (2011). B. Analogous stratigraphic sections of the Bathurst District (Goodfellow and Peter, 1996), Iberian Pyrite Belt (Tornos, 2006), Wolverine Lake (Murphy et al., 2006) and Xitieshan District illustrating the volcaniclastic and sedimentary lithofacies that characterizes these siliciclastic-felsic successions, from left to right, respectively. TG = Tetagouche Group, MNF Fm = Miramichi Nepisiguit Falls Formation, FLBB Fm = Flat Landing Boucher Brook Formation, PQ = Phyllite-Quartzite Group, VSC = Volcano Sedimentary Complex, FG = Flysch Group.

8.4. Relationship among the sedimentation, mineralization and volcanism

The presence of abundant carbonaceous schist in unit a-2 and unit b, as well as its minor amount in unit d-2, suggest periodic hiatuses in volcanism within a topographic depression. The topographic depression may represent a closed and reduced environment, and is in favor of bacterial reduction of seawater sulfate and the preservation of carbonaceous material which always play an important role in the fixing and absorption of the ore-forming material. Based on a rapid sedimentation rate of 13 cm per 1000 years (Goodfellow and Turner, 1989), the 100 m thickness of carbonaceous schist in unit a-2 should correspond to a minimum of 780,000 years (ignoring the late deformation) and represents the minimum duration of hydrothermal activity and associated felsic volcanism. This is also consistent with the age of unit b (ca. 451 Ma), and suggesting that the sedimentation of unit a-2 lasted for ca. 1 Ma, which is in agreement with the age of the mineralization at most ancient VMS deposits that lasted normally 1–2 Ma (Piercey et al., 2004). The hiatus in volcanism is always consistent with the timing of massive sulfide formation (Piercey et al., 2004). The iron-manganese chert is also evidence for the continued hydrothermal activity between the volcanic eruption and sedimentation.

Part of the sulfur was likely originated from bacterial reduction of seawater sulfate in the Xitieshan deposit (Zhu et al., 2010), a dominant mechanism for the supply of sulfur in SEDEX deposits that formed under anoxic conditions (Goodfellow, 1987; Lyons et al., 2006; Wang et al., 2009). This is consistent with the paleoclimate during the Ordovician when the oceans were stratified with an anoxic and H_2S-rich water column, such as the Bathurst (Goodfellow and Peter, 1996; Lentz, 1999; MacLellan et al., 2006; Walker and Lentz, 2006). The anoxic bottom waters environment was in favor of the ultra-large and large scale VMS deposits from the Archeozoic to the Phanerozoic (Galley et al., 2007; Goodfellow and Lydon, 2007; Hannington et al., 2005; Holland, 2005; Large et al., 2005; Leach et al., 2010).

Temperatures of mineralization at the Xitieshan deposit are estimated to have been as high as 280 °C to 360 °C (Wang et al., 2009; Wang et al., 2008), slightly higher that of the Wolverine deposit, ranging from 235 to 353 °C (Bradshaw et al., 2008), which decreased to ca. 200 °C at the initial stages of sulfide precipitation. The estimated salinities (12–18 wt.% NaCl equiv.) (Wang et al., 2009) of the hydrothermal fluids are nearly four times more to that of modern submarine hydrothermal systems or normal seawater (3.2 wt.% NaCl equiv.) (Nehlig, 1991; Rona, 1988); the higher salinities are in favor of formation of many VHMS deposits (Bradshaw et al., 2008; Lüders et al., 2001; Peter and Scott, 1988). $\delta^{34}S$ values of sulfides (pyrite, galena and sphalerite) from the Xitieshan deposit range from 0.8 to 5.4 per mil, display obviously the tower effect, suggesting that it was derived from mainly inorganic reduction of seawater sulfate and mixed with minor deep brine (Zhu et al., 2010). Traditionally, the ore forming fluids of the SEDEX deposits were derived from the seawater (Cathles, 1993; Goodfellow and Lydon, 2007). However, magmatic fluid partly contributed to the Xitieshan deposit, which evidenced from the high temperature, high salinity, intensive $\delta^{34}S$ values and containing the CO_2-fluid inclusion (Chen and Li, 2009; Chen et al., 2009; Wang et al., 2009; Zhu et al., 2010). Therefore, it is speculation that there was a deep magma chamber under the Xitieshan deposit (Fig. 16A, B). Magma upwelled along

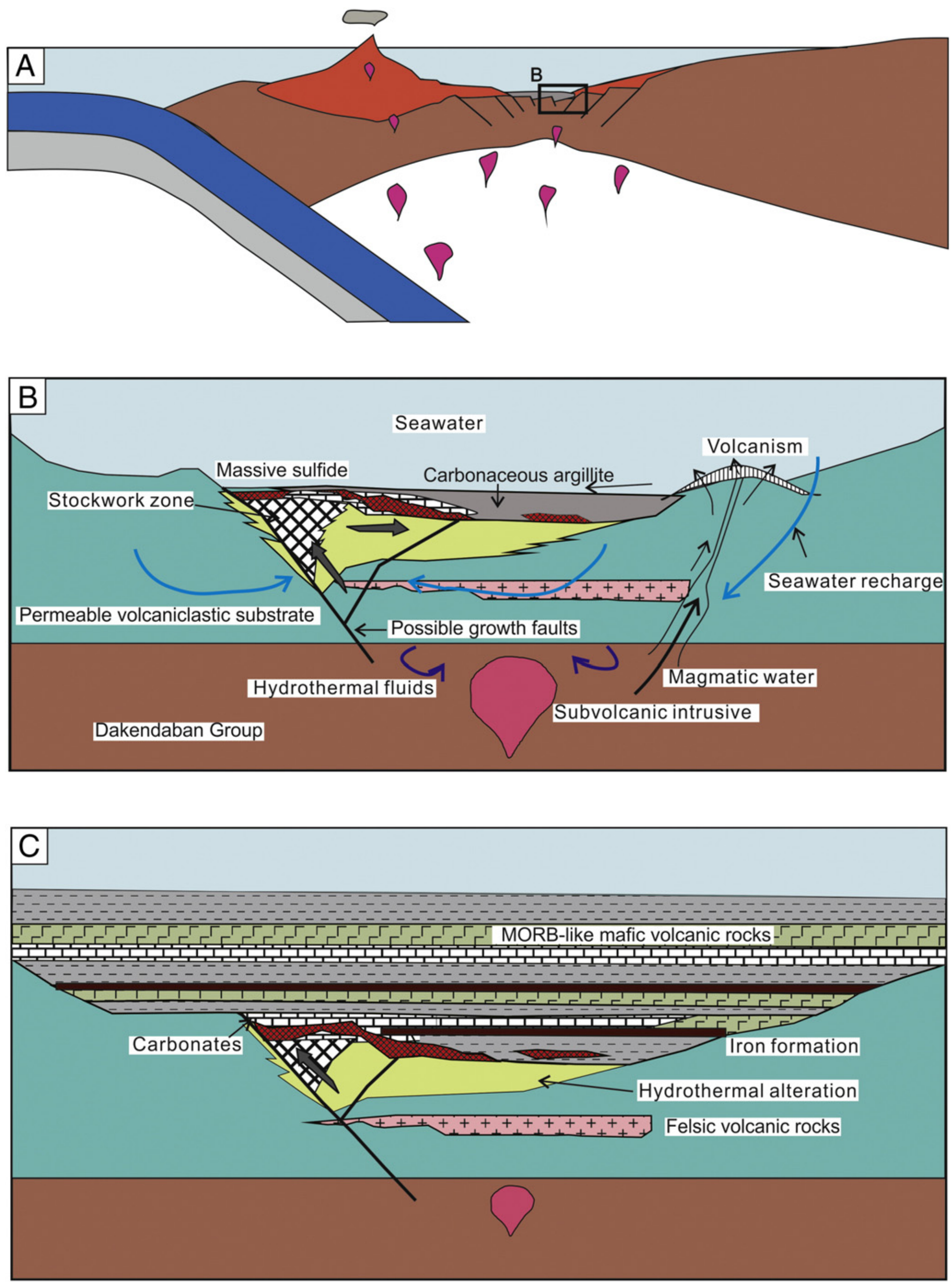

Fig. 16. Schematic block diagram illustrating the formation of the Xitieshan deposit. A. About 455 Ma, as the ocean crust continuing subduction, the subduction related island arc volcanic rocks (bimodal volcanic rocks in unit a) formed, and interpreted tectonic setting of the Xitieshan back-arc basin. B. About 452 Ma, accompanied with the initiate rifting of the back-arc basin, both the growth fault and volcanic dome controlled the secondary or third basin, the development of local topographic depressions where sulfides precipitated from hydrothermal fluids that vented onto or at the sea floor and replaced permeable volcaniclastic host rocks in the subsea floor, the hydrothermal fluids were originated from both the magma and mixture with the seawater. C. After the Xitieshan deposit forming, with increasing extension of the back-arc basin, the Xitieshan deposit was stratigraphically covered by the MORB-like in unit d. Map modified from Bradshaw et al. (2008), Wu et al. (1987) and Piercey et al. (2003).

the fault and formed bimodal volcanic rocks during the rifting stage of the back-arc basin. Sequently, abundant marine sedimentary rocks formed during the volcanic hiatus, at the same time, owing to the thermal mechanism of the deep magma chamber and residual magmatic heat, mixture with the magmatic emanation and the magma fluid raised along deep faults with lots of volatile substance (i.e., CO_2) escaping and mixing with the cold seawater during the continued upwelling, resulting in quick deposition of the mineralization fluid and formation of the massive sulfide (Fig. 16). The exhalative pipe-like complex associated with the presence of sulfide stringer veins and hydrothermal breccias and adjacent hydrothermal alteration in fractured rock beneath the base of the Xitieshan zone (Fig. 16), represent the feeder zone that provides a channel for hydrothermal fluids that precipitated massive sulfides. At the same time, these fluids reacted with permeable host rocks below the sea floor and formed the footwall alteration zone. With increasing extension of the back-arc basin, the Xitieshan deposit was stratigraphically covered by the MORB-like volcanic rocks in unit d (Fig. 16C) (Sun et al., 2012). This evolution process is similar to that of the Wolverine deposit (Piercey et al., 2002).

The Xitieshan deposit formed within a Middle to Late Ordovician back-arc marine basin. Hydrothermal venting, nearly coeval felsic volcanism and sedimentation may have occurred within the topographic depression on the sea floor during the initial rifting stage of the back-arc basin (Fig. 16). The ideal model for the Xitieshan deposit as a combination of VMS and SEDEX types (VSHMS) is presented as Fig. 16. Its typical metallogenic characteristics are: 1) both the hydrothermal fluid at the late volcanism and infiltration of seawater provided the ore-forming material; 2) both the activities of the growth fault and volcanic dome together controlled the formation of the secondary basin; 3) heat related to volcanism provided the driving force of fluid flow leading to the formation of sulfide deposits; 4) strong deformation and metamorphism during the Early Devonian orogeny (ca. 399 Ma), which resulted in the remobilization and reworking of the massive sulfides.

9. Summary and conclusions

The Xitieshan deposit occurs in the North Qaidam district, within a geologically distinct package of metamorphosed Middle to Late Ordovician bimodal volcanic and sedimentary rocks of the Tanjianshan Group that formed within a back-arc marine basin between the Qaidam and Qilian blocks. With the exception of sandy conglomerate succession (unit c), two volcanic sedimentary cycles were identified: early and late cycle from bottom to top. The Xitieshan deposit formed at the beginning of the early volcanic sedimentary cycle. The host rocks to the deposit are composed of footwall felsic volcanic rocks, volcaniclastic rocks, carbonaceous schist and carbonates. The massive sulfides are in close contact with carbonate-bearing exhalite and iron-manganese chert iron formation. Although most abundant in unit a-2 to massive sulfide, carbonaceous schist occurs throughout the hanging wall including unit a-2 and unit b, additionally present minor amounts in unit d-2, marking periodic hiatuses in volcanism. At the same time, the presence of volcaniclastic rocks interbedded with the lamellar carbonaceous schist suggests that volcanism was almost synchronous with sedimentation. Volcanism in unit a-1 helped to focus hydrothermal upflow and contributed to efficient metal deposition. The massive carbonates provided enough space for the massive sulfide lenses, and the rapid sedimentation and burial of the carbonaceous mudstone likely contributed to the large size of the Xitieshan deposit.

The primary geologic structures at the Xitieshan mining area were partly destroyed by the strong post-mineral deformation events and precluded reconstruction of the primary setting of mineralization. The ductile shear zone at the Xitieshan deposit, formed at ca. 399 Ma, was the product of collision between the Qaidam and Qilian blocks during the Early Devonian orogeny and resulted in destruction and change in the form of the orebodies. The formation age of the Xitieshan deposit can be defined at ca. 452 Ma that corresponds to a particularly fertile episode of VMS formation in the Tanjianshan Group and elsewhere in the world. Compared with other VSHMS deposits, such as the Bathurst district of Canada, the Iberian Pyrite Belt of Spain, the Wolverine volcanogenic massive sulfide deposit in Canada, there are many similarities in stratigraphy, geochemistry, and geodynamic setting and so on. Based on its tectonic setting, host-rock types, local geologic setting, metal grades, temperatures and salinities of mineralization fluid, and source of sulfur, the Xitieshan deposit is the intermedium between the SEDEX and VMS, and is classified as a VSHMS deposit in North Qaidam. In addition to the five attributes of this kind of deposits from the previous work (Bradshaw et al., 2008), the other key attributes are 1) formation stage during the periodic volcanic hiatuses, 2) association with the abundant carbonates in the host rocks, 3) mineralizing fluid originated from both the magmas and involved seawater, 4) multiple hydrothermal vent sites always coalesced together, 5) association with the FII type felsic volcanic rocks.

Acknowledgments

This contribution was financially supported by National Natural Science Foundation of China (Grant Nos. 41173066, 41072081, 40872080 and 41576040). Additional financial assistance came from Western Mining Ltd. (Grant No. 20110303), Qinghai Province, China. The authors wish to express their sincere appreciation to Yongsheng Zhong, Shengmei Duan of Western Mining Ltd., and Houyou Li, Heng Ou of 217 Team of Nonferrous Geological Prospecting Bureau, Hunan Province for access to Xitieshan drill core and outcrop, and for providing the geologic data in the form of drill logs, maps, plan sections, and unpublished reports. Steve Piercey, Sahsa Yakubchuk and Steven McCutcheon are thanked for their reviews and suggestions, which have greatly improved the manuscript. We thank journal reviewer professor Guoxiang Chi and another anonymous reviewer. Associate Editor Ibrahim Uysal is also thanked for thoughtful comments and editorial contributions.

Appendix A

A.1. Analytical methods

A.1.1. U-Pb geochronology

Each sample weighed approximately 5 kg. Samples were washed, then crushed in a jaw crusher and ground to a fine powder. The powder was panned using a Wilfley table to produce 100–200 ml of heavy mineral concentrate. The concentrate was passed through heavy liquids and a Frantz magnetic separator in a sequence of steps designed to separate minerals according to their density and magnetic susceptibility. The high quality zircons from the least magnetic high-density fractions (Romeo et al., 2006) were selected for analysis. Zircon grains were selected according to criteria of morphology and clarity using jeweler's tweezers under a microscope.

All the analyses were performed at the State Key Laboratory of Isotope Geochemistry located in the Guangzhou Institute of Geochemistry, Chinese Academy of Sciences. Using a combination of cathodoluminescence (CL) and optical microscopy, the clearest, least fractured rims of the zircon crystals were selected as suitable targets for laser ablation inductively coupled plasma mass spectrometry (LA-ICP-MS) analysis. The methodology for LA-ICP-MS is described by Tu et al. (2011). Sample mounts were placed in the two-volume sample cell flushed with Ar and He. Laser ablation was operated at a constant energy 80 mJ and at 8 Hz, with a spot diameter of 31 μm. The ablated material was carried by the He gas to an Aglient 7500a ICP-MS. Element corrections were made for mass bias drift, which was evaluated by reference to standard glass NIST 610. Temora standard was used as the age standard ($^{206}Pb/^{238}U = 416.8$ Ma)(Black et al., 2003). Trace-element concentrations were obtained by normalizing count rates for each analyzed element to those for Si, and assuming SiO_2 to be stoichiometric in zircon (Tu et al., 2011). Age calculations were made using the method of

Liu et al. (2008). Errors associated with individual analyses were calculated using the numerical error propagation method of Ludwig (2003), and are quoted at the 95% confidence level. Decay constants used are those recommended by Steiger and Jäger (1977), and compositions for initial common Pb were taken from the model of Stacey and Kramers (1975).

A.1.2. ^{40}Ar-^{39}Ar laser probe analyses

Muscovite ^{40}Ar-^{39}Ar dating were undertaken at State Key Laboratory of Isotope Geochemistry, Guangzhou Institute of Geochemistry, Chinese Academy of Sciences, Guangzhou, China, by the laser phase heating on the GVI5400® mass spectrometer. Muscovites were separated from ca. 5 kg sample, using conventional crushing, grinding, Wilfley table, heavy liquids, Frantz magnetic separation, the selected pure (purity > 99%) by stereoscopic microscope selection and ultrasonic cleaning techniques.

The samples were irradiated at China Institute of Atomic Energy (China) for 48 h. The ZBH-2506 biotite standard in granite of the Fang Shan, Beijing, with an age of 132.5 Ma, was used to monitor the fast-neutron flux. The calculated J value is 0.0117877. Analyses were corrected for blanks measured either side of five consecutive samples analyses. ^{37}Ar decay and neutron-induced interference reactions using the correction factors: $(^{39}Ar/^{37}Ar)_{Ca} = 8.984 \times 10^{-4}$, $(^{36}Ar/^{37}Ar)_{Ca} = 2.673 \times 10^{-4}$, $(^{40}Ar/^{39}Ar)_K = 5.97 \times 10^{-3}$. The data and diagrams were processed by the software ArArCALC ver2.40 (Koppers, 2002).

References

Barrie, C.T., Hannington, M.D., 1999. Classification of volcanic-associated massive sulfide deposits based on host-rock composition. Rev. Econ. Geol. 8, 1–11.

Black, L.P., Kamo, S.L., Allen, C.M., Aleinikoff, J.N., Davis, D.W., Korsch, R.J., Foudoulis, C., 2003. TEMORA 1: a new zircon standard for phanerozoic U–Pb geochronology. Chemical Geology 200, 155–170.

Bradshaw, G.D., 2003. Geology and Genesis of the Wolverine Polymetallic Volcanic Rock-hosted Massive Sulphide (VHMS) Deposit, Finlayson Lake District, Yukon, Canada Unpublished M.Sc. thesis The University of British Columbia, Vancouver, Canada (185 p).

Bradshaw, G.D., Tucker, T.L., Peter, J.M., Paradis, S., Rowins, S.M., 2001. Geology of the Wolverine polymetallic volcanic-hosted massive sulphide deposit, Finlayson Lake district, Yukon Territory, Canada. In: Emond, D.S., Weston, L.H. (Eds.), Yukon Exploration and Geology 2000, Exploration and Geological Services Division, Yukon, Indian and Northern Affairs Canada, pp. 269–287.

Bradshaw, G.D., Rowins, S.M., Peter, J.M., Taylor, B.E., 2008. Genesis of the Wolverine volcanic sediment-hosted massive sulfide deposit, Finlayson Lake district, Yukon, Canada: mineralogical, mineral chemical, fluid inclusion, and sulfur isotope evidence. Economic Geology 103, 35–60.

Bureau of Geology Mineral Resources of Qinghai Province, 1991. Regional Geology of Qinghai Province: Beijing. Geological Publishing House, pp. 315–318 (in Chinese).

Cathles, L.M., 1993. A capless 350 degrees C flow zone model to explain megaplumes, salinity variations, and high-temperature veins in ridge axis hydrothermal systems. Econ. Geol. 88, 1977–1988.

Chen, Y., Li, N., 2009. Nature of ore-fluids of intracontinental intrusion-related hypothermal deposits and its difference from those in island arcs. Acta Petrol. Sin. 25, 2477–2508 (in Chinese with English abstract).

Chen, Y., Pirajno, F., Li, N., Guo, D., Lai, Y., 2009. Isotope systematics and fluid inclusion studies of the Qiyugou breccia pipe-hosted gold deposit, Qinling Orogen, Henan province, China: implications for ore genesis. Ore Geology Reviews 35, 245–261.

de Oliveira, D.P.S., Matos, J.X., Rosa, C.J.P., Rosa, D.R.N., Figueiredo, M.O., Silva, T.P., Guimarães, F., Carvalho, J.R.S., Pinto, Á.M.M., Relvas, J.R.M.S., Reiser, F.K.M., 2011. The Lagoa Salgada orebody, Iberian Pyrite Belt, Portugal. Economic Geology 106, 1111–1128.

Downey, W.S., McCutcheon, S.R., Lentz, D.R., 2006. A physical volcanological, chemostratigraphic, and petrogenetic analysis of the Little Falls Member, Tetagouche Group, Bathurst Mining Camp, New Brunswick. Exploration and Mining Geology 15, 77–98.

Du, Y., Zhu, J., Han, X., Gu, S., 2004. From the back-arc basin to foreland basin: Ordovician-Devonian sedimentary basin and tectonic evolution in the North Qilian orogenic belt. Geological Bulletin of China 23, 911–917 in Chinese with English abstract.

Feng, Z., Li, S., Chen, R., 1997. The ore-controlling structural modle and its characteristics in the Xitieshan Pb-Zn mine of Qinghai province. Geotecton. Metallog. 21, 167–172 (in Chinese with English abstract).

Feng, Z., Sun, H., Wu, G., Wang, Y., 2010. A discussion on type of the Xitieshan Pb-Zn ore deposit, Qinghai. Geological Review 54, 501–512 (in Chinese with English abstract).

Fu, J., Liang, X., Wang, C., Jiang, Y., Zhou, Y., Pan, C., Zhong, Y., Yang, Y., Wang, Z., 2014. Timing and characteristic of provenance of the c formation in the Tanjianshan Group, Xitieshan, North Qaidam. Acta Geologica Sinica 88, 1081–1092 (in Chinese with English abstract).

Gaboury, D., Pearson, V., 2008. Rhyolite geochemical signatures and association with volcanogenic massive sulfide deposits: examples from the Abitibi Belt, Canada. Economic Geology 103, 1531–1562.

Galley, A.G., Hannington, M.D., Jonasson, I.R., 2007. Volcanogenic massive sulphide deposits. In: Goodfellow, W.D. (Ed.), Mineral Deposits of Canada: A Synthesis of Major Deposit-types, District Metallogeny, the Evolution of Geological Provinces, and Exploration Methods, Geological Association of Canada, Mineral Deposits Division, Special Publication No. 5, pp. 141–161.

Goodfellow, W.D., 1987. Anoxic stratified oceans as a source of sulphur in sediment-hosted stratiform Zn-Pb deposits (Selwyn Basin, Yukon, Canada). Chem. Geol. 65, 359–382.

Goodfellow, W.D., 2002. In: Goodfellow, W.D. (Ed.), Current understanding of the origin of massive sulphide deposits in the Bathurst Mining Camp, Northern New Brunswick 72. Geological Association of Canada, Mineral Deposits Division, pp. 1–10.

Goodfellow, W.D., Lydon, J.W., 2007. Sedimentary exhalative (Sedex) deposits. In: Goodfellow, W.D. (Ed.), Mineral Deposits of Canada: A Synthesis of Major Deposit-types, District Metallogeny, the Evolution of Geological Provinces, and Exploration Methods, 5, Geological Association of Canada, Mineral Deposits Division, Special Publication No. 5, pp. 163–183.

Goodfellow, W.D., McCutcheon, S.R., 2003. Geologic and genetic attributes of volcanic sediment-hosted massive sulfide deposits of the Bathurst Mining Camp, northern New Brunswick- a synthesis. Economic Geology Monograph 11, 245–301.

Goodfellow, W.D., Peter, J.M., 1996. Sulphur isotope composition of the Brunswick No. 12 massive sulphide deposit, Bathurst Mining Camp, New Brunswick: implications for ambient environment, sulphur source, and ore genesis. Canadian Journal of Earth Sciences 33, 231–251.

Goodfellow, W.D., Turner, R.J.W., 1989. Sulfur isotope variability in sediment-hosted massive sulfide deposits as determined using the ion microprobe SHRIMP: 1. An example from the Rammelsberg orebody - a discussion. Economic Geology 84, 451–452.

Guo, J., 2000. Structural analysis of the Tanjianshan Group in the north margin of Qaidam Block, China and its implication. Progress in Precambrian Research 23, 147–152 (in Chinese with English abstract).

Hannington, M.D., de Ronde, C.D.J., Petersen, S., 2005. Sea-floor tectonics and submarine hydrothermal systems. In: Hedenquist, J.W., Thompson, J.F.H., Goldfarb, R.J., Richards, J.P. (Eds.), Economic Geology 100th Anniversary Volume: Littelton, Colorado, USA. Society of Economic Geologists, pp. 111–141.

Hart, T.R., Gibson, H.L., Lesher, C.M., 2004. Trace element geochemistry and petrogenesis of felsic volcanic rocks association with volcanogenic massive Cu-Zn-Pb sulfide deposits. Econ. Geol. 99, 1003–1013.

Herzig, P.M., Hannington, M.D., 1995. Polymetallic massive sulfides at the modern seafloor a review. Ore Geol. Rev. 10, 95–115.

Holland, H.D., 2005. 100th anniversary special paper: sedimentary mineral deposits and the evolution of earth's near-surface environments. Economic Geology 100, 1489–1509.

Hollings, P., Stott, G., Wyman, D., 2000. Trace element geochemistry of the Meen–Dempster greenstone belt, Uchi subprovince, Superior Province, Canada: back-arc development on the margins of an Archean protocontinent. Canadian Journal of Earth Sciences 37, 1021–1038.

Hou, Z., Deng, J., Sun, H., Song, S., 1999. Volcanogenic massive sulfide deposits in China; setting, feature, and style. Explor. Min. Geol. 8, 149–175.

Inverno, C.M.C., Solomon, M., Barton, M.D., Foden, J., 2008. The Cu stockwork and massive sulfide ore of the Feitais volcanic-hosted massive sulfide deposit, Aljustrel, Iberian Pyrite Belt, Portugal: a mineralogical, fluid inclusion, and isotopic investigation. Economic Geology 103, 241–267.

Koppers, A.A.P., 2002. ArArCALC—software for 40Ar/39Ar age calculations. Comput. Geosci. 28, 605–619.

Large, R.R., 1992. Australian volcanic-hosted massive sulfide deposits; features, styles, and genetic models. Econ. Geol. 87, 471–510.

Large, R.R., Bull, S.W., McGoldrick, P.J., Walters, S., 2005. Stratiform and Strata-bound Zn-Pb-Ag Deposits in Proterozoic Sedimentary Basins, Northern Australia: Economic Geology 100th Anniversary Volume. pp. 931–963.

Leach, D.L., Bradley, D.C., Huston, D., Pisarevsky, S.A., Taylor, R.D., Gardoll, S.J., 2010. Sediment-hosted lead-zinc deposits in earth history. Econ. Geol. 105, 593–625.

Leistel, J.M., Marcoux, E., Thiéblemont, D., Quesada, C., Sánchez, A., Almodóvar, G.R., Pascual, E., Sáez, R., 1997. The volcanic-hosted massive sulphide deposits of the Iberian Pyrite Belt review and preface to the thematic issue. Mineral. Deposita 33, 2–30.

Lentz, D.R., 1998. Petrogenetic evolution of felsic volcanic sequences associated with Phanerozoic volcanic-hosted massive sulphide systems: the role of extensional geodynamics. Ore Geology Reviews 12, 289–327.

Lentz, D.R., 1999. Petrology, geochemistry, and oxygen isotope interpretation of felsic volcanic and related rocks hosting the Brunswick 6 and 12 massive sulfide deposits (Brunswick Belt), Bathurst mining camp, New Brunswick, Canada. Economic Geology 94, 57–86.

Lentz, D.R., McCutcheon, S.R., 2006. The Brunswick No. 6 massive sulfide deposit, Bathurst Mining Camp, northern New Brunswick, Canada: a synopsis of the geology and hydrothermal alteration system. Exploration and Mining Geology 15, 1–34.

Lesher, C.M., Goodwin, A.M., Campbell, I.H., Gorton, M.P., 1986. Trace-element geochemistry of ore-associated and barren, felsic metavolcanic rocks in the Superior Province, Canada. Canadian Journal of Earth Sciences 23, 222–237.

Li, F., Wu, Z., Li, B., 2007. Recognition on formation age of the Tanjianshan Group on the northern margin of the Qaidam basin and its geological significance. Geotecton. Metallog. 31, 226–233 (in Chinese with English abstract).

Li, F., Jian, R., Zhao, X., 2009. Geochemical characteristics and formation setting of silicolites in the Xitieshan deposit, Qinghai Province. Journal of Kunming University of Science and Technology (Science and Technology) 34, 1–9 (in Chinese with English abstract).

Liu, Y., Hu, Z., Gao, S., Günther, D., Xu, J., Gao, C., Chen, H., 2008. In situ analysis of major and trace elements of anhydrous minerals by LA-ICP-MS without applying an internal standard. Chem. Geol. 257, 34–43.

Lüders, V., Pracejus, B., Halbach, P., 2001. Fluid inclusion and sulfur isotope studies in probable modern analogue Kuroko-type ores from the JADE hydrothermal field (Central Okinawa Trough, Japan). Chem. Geol. 173, 45–58.

Ludwig, K.R., 2003. User's Manual for Isoplot/EX version 3.00: A Geochronological Tool Kit for Microsoft Excel: Brkeley Geochronology Center, Special Publication. pp. 1–70.

Lyons, T.W., Gellatly, A.M., McGoldrick, P.J., Kah, L.C., 2006. Proterozoic sedimentary exhalative (SEDEX) deposits and links to evolving global ocean chemistry. In: Kesler, S.E., Ohmoto, H. (Eds.), Evolution of Early Earth's Atmosphere, Hydrosphere, and Biosphere - Constrains from Ore Deposits. Geological Society of America Memoirs vol. 198, pp. 169–184.

MacLellan, K.L., Lentz, D.R., McClenaghan, S.H., 2006. Petrology, geochemistry, and genesis of the Copper zone at the Brunswick No. 6 volcanogenic massive sulfide Deposit, Bathurst Mining Camp, New Brunswick, Canada. Exploration and Mining Geology 15, 53–75.

Mao, J., Zhang, Z., Yang, J., Zuo, G., Zhang, Z., Ye, D., Wang, Z., Ren, F., Zhang, Y., Peng, C., Liu, Y., Jiang, M., 2003. Metallogenic Series and Prospecting Assessment of Copper, Gold, Iron and Tungsten Polymetallic Ore Deposits in the West Sector of the Northern Qilian Mountains: Beijing. Geological Publishing House (437 p in Chinese).

McClenaghan, S.H., Lentz, D.R., Beaumont-Smith, C.J., 2006. The gold-rich Louvicourt volcanogenic massive sulfide deposit, New Brunswick: a Kuroko analogue in the Bathurst Mining Camp. Exploration and Mining Geology 15, 127–154.

Meng, F., Zhang, J., Yang, J., 2005. Tectono-thermal event of post-HP/UHP metamorphism in the Xitieshan area of the North Qaidam Mountains, western China: isotopic and geochemical evidence of granite and gneiss. Acta Petrologica Sinica 21, 45–56.

Mireku, L.K., Stanley, C.R., 2006. Lithogeochemistry and hydrothermal alteration at the Halfmile Lake south deep zone, a volcanic-hosted massive sulfide deposit, Bathurst Mining Camp, New Brunswick. Exploration and Mining Geology 15, 177–199.

Mitjavila, J., Martí, J., Soriano, C., 1997. Magmatic evolution and tectonic setting of the Iberian Pyrite Belt volcanism. J. Petrol. 38, 727–755.

Möller, A., O'Brien, P.J., Kennedy, A., Kröner, A., 2003. Linking Growth Episodes of Zircon and Metamorphic Textures to Zircon Chemistry: An Example from the Ultrahigh-temperature Granulites of Rogaland (SW Norway). vol. 220. Geological Society, London, Special Publications, pp. 65–81.

Murphy, D.C., 1997. Stratigraphic Framework for Syngenetic Mineral Occurrences, Yukon-Tanana Terrane south of Finlayson Lake: A Progress Report, Yukon Exploration and Geology 1997. Exploration and Geological Services Division, Yukon, Indian and Northern Affairs Canada, pp. 51–58.

Murphy, D.C., Mortensen, J.K., Piercey, S.J., Orchard, M.J., Gehrels, G.E., 2006. Mid-Paleozoic to early Mesozoic tectonostratigraphic evolution of Yukon-Tanana and Slide Mountain terranes and affiliated overlap assemblages, Finlayson Lake massive sulphide district, southeastern Yukon. In: Colpron, M., Nelson, J.L. (Eds.), Paleozoic Evolution and Metallogeny of Pericratonic Terranes at the Ancient Pacific Margin of North America, Canadian and Alaskan Cordillera, Geological Association of Canada, Special Paper. vol. 45, pp. 75–105.

Nehlig, P., 1991. Salinity of oceanic hydrothermal fluids: a fluid inclusion study. Earth and Planetary Science Letters 102, 310–325.

Peter, J.M., Goodfellow, W.D., 1996. Mineralogy, bulk and rare earth element geochemistry of massive sulphide-associated hydrothermal sediments of the Brunswick Horizon, Bathurst Mining Camp, New Brunswick. Canadian Journal of Earth Sciences 33, 252–283.

Peter, J.M., Scott, S.D., 1988. Mineralogy, composition, and fluid inclusion microthermometry of sea-floor hydrothermal deposits in the southern trough of Guaymas Basin, Gulf of California. The Canadian Mineralogist 26, 567–587.

Piercey, S., 2010. An overview of petrochemistry in the regional exploration for volcanogenic massive sulphide (VMS) deposits. Geochemistry: Exploration, Environment, Analysis 10, 119–136.

Piercey, S.J., 2011. The setting, style, and role of magmatism in the formation of volcanogenic massive sulfide deposits. Mineral. Deposita 46, 449–471.

Piercey, S.J., Paradis, S., Murphy, D.C., Mortensen, J.K., 2001. Geochemistry and paleotectonic setting of felsic volcanic rocks in the Finlayson Lake volcanic-hosted massive sulfide district, Yukon, Canada. Economic Geology 96, 1877–1905.

Piercey, S.J., Mortensen, J.K., Murphy, D.C., Paradis, S., Creaser, R.A., 2002. Geochemistry and tectonic significance of alkalic mafic magmatism in the Yukon-Tanana terrane, Finlayson Lake region, Yukon. Canadian Journal of Earth Sciences 39, 1729–1744.

Piercey, S.J., Mortensen, J.K., Creaser, R.A., 2003. Neodymium isotope geochemistry of felsic volcanic and intrusive rocks from the Yukon–Tanana Terrane in the Finlayson Lake Region, Yukon, Canada. Canadian Journal of Earth Sciences 40, 77–97.

Piercey, S.J., Murphy, D.C., Mortensen, J.K., Creaser, R.A., 2004. Mid-Paleozoic initiation of the northern Cordilleran marginal backarc basin: geologic, geochemical, and neodymium isotope evidence from the oldest mafic magmatic rocks in the Yukon-Tanana terrane, Finlayson Lake district, southeast Yukon, Canada. Geological Society of America Bulletin 116, 1087–1106.

Piercey, S.J., Peter, J.M., Mortensen, J.K., Paradis, S., Murphy, D.C., Tucker, T.L., 2008. Petrology and U-Pb geochronology of footwall porphyritic rhyolites from the Wolverine volcanogenic massive sulfide deposit, Yukon, Canada: implications for the genesis of massive sulfide deposits in continental margin environments. Economic Geology 103, 5–33.

Relvas, J.M.R.S., Barriga, F.J.A.S., Ferreira, A., Noiva, P.C., Pacheco, N., Barriga, G., 2006a. Hydrothermal alteration and mineralization in the Neves-Corvo volcanic-hosted massive sulfide deposit, Portugal. I. Geology, mineralogy, and geochemistry. Economic Geology 101, 753–790.

Relvas, J.M.R.S., Barriga, F.J.A.S., Longstaffe, F.J., 2006b. Hydrothermal alteration and mineralization in the Neves-Corvo volcanic-hosted massive sulfide deposit, Portugal. II. Oxygen, hydrogen, and carbon isotopes. Economic Geology 101, 791–804.

Romeo, I., Lunar, R., Capote, R., Quesada, C., Dunning, G.R., Piña, R., Ortega, L., 2006. U–Pb age constraints on Variscan magmatism and Ni–Cu–PGE metallogeny in the Ossa–Morena Zone (SW Iberia). J. Geol. Soc. 163, 837–846.

Rona, P.A., 1988. Hydrothermal mineralization at oceanic ridges. Can. Mineral. 26, 431–465.

Rubatto, D., Gebauer, D., 2000. Use of cathodoluminescence for U-Pb zircon dating by ion microprobe: some examples from the Western Alps. In: Pagel, M., Barbin, V., Blanc, P., Ohnenstetter, D. (Eds.), Cathodoluminescence in Geosciences. Springer, Berlin Heidelberg, pp. 373–400.

Sáez, R., Pascual, E., Toscano, M., Almodóvar, G.R., 1999. The Iberian type of volcano-sedimentary massive sulphide deposits. Mineral. Deposita 34, 549–570.

Sánchez-España, J., Velasco, F., Yusta, I., 2000. Hydrothermal alteration of felsic volcanic rocks associated with massive sulphide deposition in the northern Iberian Pyrite Belt (SW Spain). Appl. Geochem. 15, 1265–1290.

Shi, R., Yang, J., Wu, C., Iizuka, T., Hirata, T., 2006. Island arc volcanic rocks in the north Qaidam UHP belt, northern Tibet plateau: evidence for ocean–continent subduction preceding continent–continent subduction. Journal of Asian Earth Sciences 28, 151–159.

Soriano, C., Marti, J., 1999. Facies analysis of volcano-sedimentary successions hosting massive sulfide deposits in the Iberian pyrite belt, Spain. Economic Geology 94, 867–882.

Staal, C.R.V., Winchester, J.A., Bédard, J.H., 1991. Geochemical variations in Middle Ordovician volcanic rocks of the northern Miramichi Highlands and their tectonic significance. Can. J. Earth Sci. 28, 1031–1049.

Stacey, J.S., Kramers, J.D., 1975. Approximation of terrestrial lead isotope evolution by a two-stage model. Earth Planet. Sci. Lett. 26, 207–221.

Steiger, R.H., Jäger, E., 1977. Subcommission on geochronology: convention on the use of decay constants in geo- and cosmochronology. Earth and Planetary Science Letters 36, 359–362.

Stolz, A.J., 1995. Geochemistry of the Mount Windsor Volcanics: implications for the tectonic setting of Cambro-Ordovician volcanic-hosted massive sulfide mineralization in northeastern Australia. Economic Geology 90, 1080–1097.

Sun, H., Zhao, L., Wu, G., Ning, J., Chen, Q., Jiang, C., 2012. Metallogenic tectonic setting and ore-finding potential of Xitieshan massive sulfide lead-zinc deposit: evidence from lithochemistry and geochemistry of ore-hosted volcanic strata Tanjianshan Group. Acta Petrologica Sinica 28, 652–664 (in Chinese with English abstract).

Tang, L., Jin, Z., Dai, J., Zhang, M., Zhang, B., 2002. Regional fault systems of Qaidam basin and adjacent orogenic belts. Earth Sci. 27, 676–682 (in Chinese with English abstract).

Taylor, B., Martinez, F., 2003. Back-arc basin basalt systematics. Earth Planet. Sci. Lett. 210, 481–497.

Thiéblemont, D., Pascual, E., Stein, G., 1997. Magmatism in the Iberian Pyrite Belt: petrological constraints on a metallogenic model. Mineralium Deposita 33, 98–110.

Tornos, F., 2006. Environment of formation and styles of volcanogenic massive sulfides: the Iberian Pyrite Belt. Ore Geology Reviews 28, 259–307.

Tornos, F., Solomon, M., Conde, C., Spiro, B.F., 2008. Formation of the Tharsis massive sulfide deposit, Iberian Pyrite Belt: geological, lithogeochemical, and stable isotope evidence for deposition in a brine pool. Economic Geology 103, 185–214.

Tu, X., Zhang, H., Deng, W., Ling, M., Liang, H., Liu, Y., Sun, W., 2011. Application of RESOlution laser ablation ICPMS in trace element analyses. Geochemica 40, 83–98 (in Chinese with English abstract).

van Staal, C.R., Fyffe, L.R., Langton, J.P., McCutcheon, S.R., 1992. The Ordovician Tetagouche Group, Bathurst Camp, northern New Brunswick, Canada; history, tectonic setting and distribution of massive-sulfide deposits. Exploration and Mining Geology 1, 93–103.

Walker, J.A., Carroll, J.I., 2006. The Camelback Zn-Pb-Cu deposit: a recent discovery in the Bathurst Mining Camp, New Brunswick, Canada. Exploration and Mining Geology 15, 201–220.

Walker, J.A., Graves, G., 2006. The Mount Fronsac north volcanogenic massive sulfide deposit: a recent discovery in the Bathurst Mining Camp, New Brunswick. Exploration and Mining Geology 15, 221–240.

Walker, J.A., Lentz, D.R., 2006. The flat landing brook Zn-Pb-Ag massive sulfide deposit, Bathurst Mining Camp, New Brunswick, Canada. Exploration and Mining Geology 15, 99–125.

Wan, Y., Xu, Z., Yang, J., Zhang, J., 2001. Ages and compositions of the Precambrian high-grade basement of the Qilian terrane and its adjacent areas. Acta Geologica Sinica 75, 375–384.

Wang, J., Huang, Y., Fu, R., 2000. The recognition on a few key geological problems of Xitieshan mine area, in Qinghai province. Mineral Resources and Geology 14, 11–15 (in Chinese with English abstract).

Wang, H., Lu, S., Yuan, G., Xin, H., Zhang, B., Wang, Q., Tian, Q., 2003. Tectonic setting and age of the Tanjianshan Group on the northern margin of the Qaidam basin. Geological Bulletin of China 22, 487–493 in Chinese with English abstract.

Wang, L., Zhu, X., Wang, J., Deng, J., Wang, Y., Zhu, H., 2008. Study on fluid inclusions of the sedimentary exhalative system (SEDEX) in Xitieshan lead-zinc deposit. Acta Petrol. Sin. 24, 2433–2440 (in Chinese with English abstract).

Wang, L., Peng, Z., Zhu, X., Deng, J., Wang, Y., Zhu, H., 2009. Source and evolution of ore-fluid of the Xitieshan sedimentary-exhalative lead-zinc system, Qinghai province: Evidence from fluid inclusion and isotope geochemistry. Acta Petrologica Sinica 25, 3007–3015 (in Chinese with English abstract).

Wang, C., Deng, J., Carranza, E.J.M., Lai, X., 2013. Nature, diversity and temporal–spatial distributions of sediment-hosted Pb-Zn deposits in China. Ore Geol. Rev. 56, 327–351.

Wills, A.O., Lentz, D.R., Roy, G., 2006. Chemostratigraphy at the Brunswick No. 6 volcanic-sediment-hosted massive sulfide deposit, New Brunswick: resolving geometry from drill core in deformed felsic volcanic rocks. Exploration and Mining Geology 15, 35–51.

Wu, J., Ren, B., Zhang, M., Gao, D., Zhao, T., Zhang, H., Song, Z., Zhang, Q., 1987. The Genetic Type and Geological Characteristics of the Xitieshan Massive Sulphide Deposit,

Qinghai: Bulletin of the Xi'an Institute of Geology and Mineral Resource. vol. 20 pp. 1–88 (in Chinese with English abstract).
Wu, G., Sun, H., Feng, Z., Fan, J., Lu, J., Wang, Y., 2010. The paleotectonic setting of Xitieshan lead-zinc deposit. Geochemica 39, 229–239 (in Chinese with English abstract).
Xu, Z., Yang, J., Wu, C., Li, H., Zhang, J., Qi, X., Song, S., Qiu, H., 2006. Timing and mechanism of formation and exhumation of the northern Qaidam ultrahigh-pressure metamorphic belt. J. Asian Earth Sci. 28, 160–173.
Yang, J., Wu, C., Zhang, J., Shi, R., Meng, F., Wooden, J., Yang, H., 2006. Protolith of eclogites in the north Qaidam and Altun UHP terrane, NW China: earlier oceanic crust? Journal of Asian Earth Sciences 28, 185–204.
Zhang, Z., Xia, W., Zhang, W., Feng, Z., 1995. Organic inclusions of Xitieshan lead-zinc deposit and their significance. Earth Science 20, 225–230 (in Chinese with English abstract).
Zhang, D., Wang, F., Li, D., Feng, C., She, H., Li, J., 2005. Two types of massive sulfide deposits on northern margin of Qaidam basin, Qinghai Province: I. Xitieshan style SEDEX lead-zinc deposit. Mineral Deposit 24, 471–480 (in Chinese with English abstract).
Zhang, J., Yang, J., Meng, F., Wan, Y., Li, H., Wu, C., 2006. U–Pb isotopic studies of eclogites and their host gneisses in the Xitieshan area of the north Qaidam mountains, western China: new evidence for an early Paleozoic HP–UHP metamorphic belt. Journal of Asian Earth Sciences 28, 143–150.
Zhang, J., G, M.C., Meng, F., Wan, Y., Tung, K., 2008. Polyphase tectonothermal history recorded in granulitized gneisses from the north Qaidam HP/UHP metamorphic terrane, western China: evidence from zircon U-Pb geochronology. Geological Society of America Bulletin 120, 732–749.
Zhang, J., Mattinson, C.G., Meng, F., Yang, H., Wan, Y., 2009. U–Pb geochronology of paragneisses and metabasite in the Xitieshan area, north Qaidam Mountains, western China: constraints on the exhumation of HP/UHP metamorphic rocks. Journal of Asian Earth Sciences 35, 245–258.
Zhao, F., Guo, J., Li, H., 2003. Geological characteristics and isotopic age of the Tanjianshan Group along north margin of Qaidam basin. Geological Bulletin of China 22, 28–31 (in Chinese with English abstract).
Zhu, X., Wang, L., Zhu, G., Deng, J., Fan, J., 2010. Characteristics of sulfur isotope geochemistry of Xitieshan lead-zinc deposit, Qinghai: the mixing of sulfurs from hydrothermal and seawater. Acta Petrologica Sinica 26, 657–666 in Chinese with English abstract.